J. Fluid Mech. (2004), *vol.* 500, *pp.* 313–347.
DOI: 10.1017/S0022112003007365 Printed in the United Kingdom

Secondary Bjerknes forces between two bubbles and the phenomenon of acoustic streamers

By NIKOLAOS A. PELEKASIS[1]†, ALEXANDRA GAKI[1], ALEXANDER DOINIKOV[2] AND JOHN A. TSAMOPOULOS[1]

[1]Laboratory of Computational Fluid Dynamics, Department of Chemical Engineering, University of Patras, Patras, Greece

[2]Institute of Nuclear Problems, Byelorussia State University, Minsk, Belarus

(Received 7 May 2002 and in revised form 16 September 2003)

The translational velocities of two spherical gas bubbles oscillating in water, which is irradiated by a high-intensity acoustic wave field, are calculated. The two bubbles are assumed to be located far enough apart so that shape oscillations can be neglected. Viscous effects are included owing to the small size of the bubbles. An asymptotic solution is obtained that accounts for the viscous drag on each bubble, for large Re based on the radial part of the motion, in a form similar to the leading-order prediction by Levich (1962), $C_D = 48/Re_T$; $Re_T \to \infty$ based on the translational velocity. In this context the translational velocity of each bubble, which is a direct measure of the secondary Bjerknes force between the two bubbles, is evaluated asymptotically and calculated numerically for sound intensities as large as the Blake threshold. Two cases are examined. First, two bubbles of unequal size with radii on the order of 100 μm are subjected to a sound wave with amplitude $P_A < 1.0$ bar and forcing frequency $\omega_f = 0.51\omega_{10}$, so that the second harmonic falls within the range defined by the eigenfrequencies of the two bubbles, $\omega_{10} < 2\omega_f < \omega_{20}$. It is shown that their translational velocity changes sign, becoming repulsive as P_A increases from 0.05 to 0.1 bar due to the growing second harmonic, $2\omega_f$, of the forcing frequency. However, as the amplitude of sound further increases, $P_A \approx 0.5$ bar, the two bubbles attract each other due to the growth of even higher harmonics that fall outside the range defined by the eigenfrequencies of the two bubbles. Second, the case of much smaller bubbles is examined, radii on the order of 10 μm, driven well below resonance, $\omega_f/2\pi = 20$ kHz, at very large sound intensities, $P_A \approx 1$ bar. Numerical simulations show that the forces between the two bubbles tend to be attractive, except for a narrow region of bubble size corresponding to a nonlinear resonance related to the Blake threshold. As the distance between them decreases, the region of repulsion is shifted, indicating sign inversion of their mutual force. Extensive numerical simulations indicate the formation of bubble pairs with constant average inter-bubble distance, consisting of bubbles with equilibrium radii determined by the primary and secondary resonance frequencies for small and moderate sound amplitudes or by the Blake threshold for large sound amplitudes. It is conjectured that in experiments where 'acoustic streamers' are observed, which are filamentary structures consisting of bubbles that are aligned and move rapidly in a cavitating fluid at nearly constant distances from each other, bubbles with size determined by the Blake threshold are predominant

† Author to whom correspondence should be addressed. Present address: Laboratory of Fluid Mechanics & Turbomachinery, Department of Mechanical & Industrial Engineering, University of Thessaly, Volos, 38334, Greece; pel@uth.gr

because those with size determined by linear resonance are larger and therefore become unstable due to shape oscillations.

1. Introduction

The behaviour of bubble populations in a cavitating fluid is of fundamental importance in damage prevention and, if controlled, can be applied to enhance gas–liquid separations (Leighton 1994). Experimental investigations have indicated the possibility of coalescence and breakup, but also the formation of stable bubble clusters where bubble separation is comparable to or much larger than the bubble radius, Kobelev, Ostrovsky & Sutin (1979), Crum & Nordling (1972), Ohl *et al.* (1999). The intriguing aspect of these findings is that they occur when the forcing frequency is outside the range defined by the two natural frequencies for volume oscillations of the two bubbles, in which case the classical theory proposed by Bjerknes (1906) predicts attraction and eventually coalescence.

Two of the most widely known patterns observed in bubble populations are those of 'bubble grapes' and 'acoustic streamers'. The former is constituted of a large number of bubbles clustered together at distances comparable to their radius under the influence of an acoustic pressure wave with frequency, ω_f, higher than the individual frequencies for volume oscillations, ω_{10}, ω_{20}, of the bubbles (driving above resonance) (Kobelev *et al.* 1979). Doinikov & Zavtrak (1995), following earlier ideas by Zabolotskaya (1984) and accounting for multiple scattering in the context of linear analysis, were able to show that the Bjerknes force between two bubbles driven above resonance can change sign as the distance between them decreases. This is a result of the fact that the eigenfrequencies for volume oscillations of the two bubbles increase as they approach each other, a direct effect of multiple scattering of sound, until, when their distance becomes small enough, the forcing frequency, ω_f, falls inside the interval defined by ω_{10}, ω_{20},and the bubbles start repelling each other. In this fashion the two bubbles tend to eventually form a stable pair without ever coalescing or shifting away from each other. This is a plausible mechanism for the formation of 'bubble grapes', which are normally observed for moderate acoustic disturbances (Kobelev *et al.* 1979), that can be understood in the context of linear theory. A similar sign inversion mechanism leading to a stable equilibrium distance between the two bubbles was discovered by Barbat, Ashgriz & Liu (1999) for near resonant pairs of bubbles in weak fields.

Another quite well known pattern is that of 'acoustic streamers', figure 1, which is observed when liquid solutions are insonated with very high-amplitude sound waves whose frequency is below the natural frequency for volume oscillations (driving below resonance) of the bubbles (Crum & Nordling 1972; Ohl *et al.* 1999). In this context, bubbles whose size is on the order of several micrometres are often seen to form filamentary structures where each one of them is moving rapidly, while the distance between them remains constant and much larger than their average radius (Mettin *et al.* 1997). This pattern is quite stable and persists for a long time without any significant bubble coalescence or breakup despite the high intensity of the imposed sound field. In an effort to explain the mechanism behind the formation of acoustic streamers, Mettin *et al.* (1997), studied the interaction between two spherical bubbles, whose separation distance ($\sim$1 mm) remains much larger than their radius ($\sim$10 μm), driven below resonance in a sound field of very large amplitude (close to the Blake

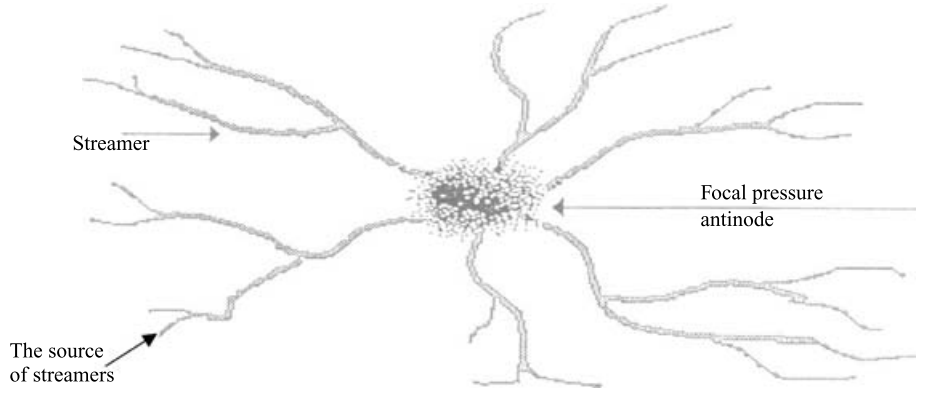

FIGURE 1. Photographic image of acoustic streamers reproduced, with permission from Elsevier, from Leighton (1994, figure 4.25, p. 351).

threshold). Using the classical form of the Bjerknes force between two bubbles, averaged over the period of the forcing, and neglecting viscous effects as well as every other form of dissipation, they were able to show that a sign inversion in the Bjerknes force arises as the distance between them decreases. This is a result of a nonlinear resonance associated with the Blake threshold. Oguz & Prosperetti (1990) employed a nonlinear model for radial oscillations of two bubbles and found sign inversion of the interaction force as the amplitude of the sound wave increases, when they are driven below resonance at nearly half their natural frequency for volume oscillations. This effect is due to the appearance of the second harmonic of the forcing frequency, which lies within the interval defined by the two individual frequencies for volume oscillations, and prevents the two bubbles from coalescing. In the same parameter range, radius 100 μm, Pelekasis & Tsamopoulos (1993*a*, *b*) extended the above study to account for shape oscillations of the two bubbles, thus allowing for smaller distances between them. In this fashion they predicted sign inversion when the forcing frequency ω_f is within the range, ω_{10}, ω_{20}, defined by the two natural frequencies. As the amplitude of the sound wave increases they observed either breakup due to intense shape oscillations or violent collapse due to transient cavitation. Their study, however, does not account for any kind of energy dissipation which would, probably, allow the simulations to proceed further and exhibit some of the effects reported by Oguz & Prosperetti.

The present study is an attempt to identify the mechanism responsible for the formation of acoustic streamers. For this reason, and in view of the large separation distance between bubbles compared to the bubble radius, we will concentrate on the radial and translational part of the motion, neglecting higher-order spherical harmonics and thus taking the bubble shape to remain spherical. In addition, due to their small size, the Reynolds number of the flow based on the radial motion of the bubbles, $Re = \rho R^2 \omega_f / \mu$, can be finite or even an $O(1)$ quantity, in which case viscous effects cannot be neglected in either the radial or the translational part of the bubbles' motion; R is the bubble radius and ρ, μ, the density and viscosity of the surrounding fluid, respectively. For example, $Re \approx 3$ for an air bubble with equilibrium radius on the order of 5 μm undergoing radial oscillations in water in which an acoustic pressure disturbance is applied with frequency $\omega_f / 2\pi = 20$ kHz, a situation normally encountered in acoustic cavitation experiments where acoustic streamers appear. Consequently, viscous dissipation affects the total interaction forces

on the two bubbles, the secondary Bjerknes forces, which now are not opposite in sign and equal in magnitude. A wide range of sound amplitudes is covered in the results reported here in an effort to unify the mechanisms proposed by Oguz & Prosperetti and Mettin *et al.* (1997). In this fashion a full account of the effect of nonlinearity is presented. In order to obtain an independent check on our numerical calculations, place our work in the context of previous studies and provide a simplified formula for the secondary Bjerknes force between two bubbles that includes viscous dissipation and that can be incorporated in a particle-type numerical scheme calculating the dynamics of large bubble populations, an asymptotic solution was obtained that is valid for a large range of sound amplitudes, at least for the initial stages of the interaction, when *Re* based on the radial motion of the two bubbles is large.

The approach adopted for the radial and translational parts of the motion is presented in §§ 2.1, 2.2. The Keller–Miksis (1980) model is used for the description of the radial motion, which allows for compressibility in the far field of the surrounding fluid. Once the radial motion is solved for, it is introduced as input in the equations describing the translational part via a vector potential. Then, in § 3 the numerical methodology is outlined. In § 4 an asymptotic solution is presented that is valid for a time interval that is not very large, when the Reynolds number of the radial motion becomes asymptotically large. The validity of the asymptotic solution is demonstrated by calculating the dynamic interaction between two relatively large bubbles, with equilibrium radii R_{10}, $R_{20} \sim 100\,\mu\text{m}$, for which *Re* of the radial motion is large, § 5.1. In § 5.2 the interaction between two smaller bubbles, equilibrium radii R_{10}, $R_{20} \sim 10\,\mu\text{m}$, is examined numerically. The *Re* characterizing the radial motion of bubbles of this size is now much smaller. Nevertheless, this seems to be a more relevant flow situation, as far as the phenomenon of acoustic streamers is concerned, see Ohl *et al.* (1999). The mechanisms proposed by Oguz & Prosperetti and Mettin *et al.* (1997) are tested against the findings of the present study by identifying the regions on the plane that is defined by the equilibrium radii of the two bubbles for which stable pairs of the two bubbles are formed. To this end we extend the recent study on bubble–bubble interaction by Barbat *et al.* (1999) and Harkin, Kaper & Nadim (2001). Finally, in § 6 conclusions are drawn regarding the validity of the two mechanisms, the limitations of these theories as well as those of the present one are discussed and directions for future research are proposed.

2. Problem formulation

We examine the dynamic interaction of two oscillating bubbles with relatively small size, figure 2, making viscous dissipation in the liquid phase important, i.e. the Reynolds number is finite. We are primarily interested in studying the phenomenon of acoustic streamers which is often observed in cavitating fluids, in which case the amplitude of the sound field is taken to be large, $\varepsilon = O(1)$. We investigate the dynamics that determine the formation of this pattern in bubble populations, at the level of bubble–bubble interaction. For this reason, and assuming a large separation distance between bubbles compared to the bubble radius, we concentrate on the radial and translational part of the motion, neglecting higher-order spherical harmonics, thus taking the bubble shape to remain spherical. Ignoring gravitational forces, the flow in the suspending medium, water in our case, is governed by the equation of motion

$$\rho \frac{\mathrm{D}\boldsymbol{u}^*}{\mathrm{D}t^*} = -\nabla P^* + \nabla \cdot \boldsymbol{T}^* \tag{2.1}$$

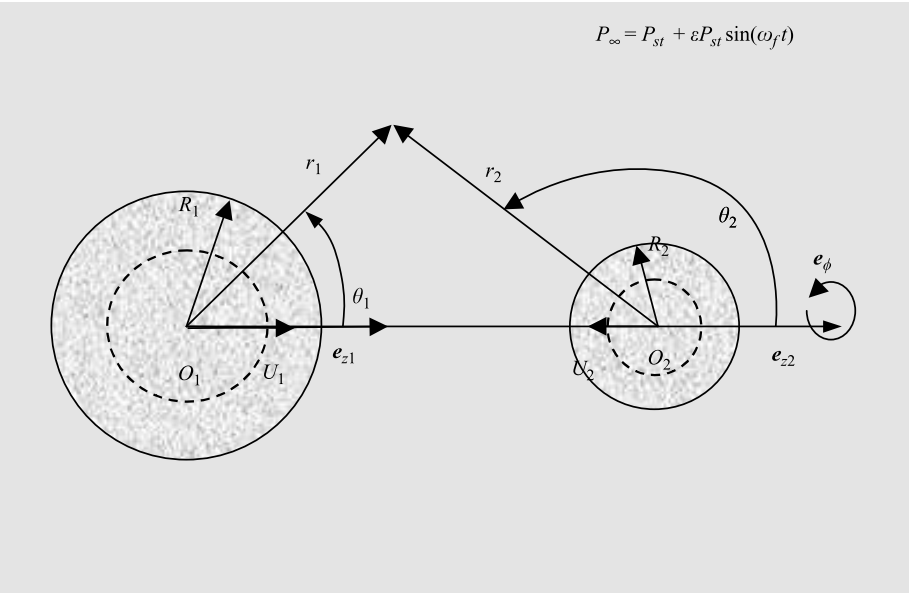

FIGURE 2. Schematic diagram of the flow configuration.

with the boundary conditions for zero shear stress, normal stress balance and the kinematic condition at the two interfaces,

$$\boldsymbol{n}_i \cdot \boldsymbol{T}^* \cdot \boldsymbol{t}_i = 0, \tag{2.2}$$

$$P^*_{gi} + P^*_u - P^* = -\boldsymbol{n}_i \cdot \boldsymbol{T}^* \cdot \boldsymbol{n}_i + \sigma \nabla \cdot \boldsymbol{n}_i, \tag{2.3}$$

$$\boldsymbol{u}^* \cdot \boldsymbol{n}_i = J^*_i, \tag{2.4}$$

the condition that the velocity field vanishes in the far field

$$\boldsymbol{r}^* \to \infty, \quad \boldsymbol{u}^* \to 0, \tag{2.5}$$

while the flow is induced by a sinusoidal variation of the pressure in the far field,

$$P^*_\infty = P^*_{st} + \varepsilon P^*_{st}\sin(\omega_f t^*). \tag{2.6}$$

In the above equations as well as in the ones to follow, asterisks indicate variables with dimensions whereas bold symbols indicate vectorial and tensorial quantities. Thus, $\boldsymbol{u}^*$ and $\boldsymbol{T}^*$ signify the velocity vector and the deviatoric stress tensor in the bulk of the liquid, J^*_i, $\boldsymbol{n}^*_i$, $\boldsymbol{t}^*_i$ and $\nabla \cdot \boldsymbol{n}_j$ denote the normal velocity, the normal and tangent vectors and the curvature of each bubble's interface with water, and P^*_{gi}, P^*_u, P^*, P^*_{st} and P^*_∞ denote the gas and vapour pressure inside the bubble, the total pressure in the water phase at the gas–water interfaces, the static pressure and the pressure at infinity in the liquid, respectively. Moreover, t^*, $\boldsymbol{r}^*$ are the dimensional time and position vector, ρ, σ are the density of water and interfacial tension between water and air and ε, ω_f, are the amplitude and the forcing frequency of the disturbance. Since, as will be seen in the following, the radial part of the motion is compressible in the far field, the components of the deviatoric stress tensor are defined as

$$T^*_{kl} = \mu\left[\left(\frac{\partial u^*_k}{\partial x^*_l} + \frac{\partial u^*_l}{\partial x^*_k}\right) - \frac{2}{3}\frac{\partial u^*_k}{\partial x^*_l}\delta_{kl}\right], \tag{2.7}$$

with μ denoting the viscosity of the surrounding fluid and x_i^* the dimensional Cartesian coordinates. Due to the compressibility of the gas inside the bubbles the primary effect of changing the far-field pressure is that both bubbles undergo radial oscillations. The translational motion of the bubbles is a result of their interaction and, due to the large initial distance between them compared to their equilibrium radii, $L_0 \gg R_{i0}$, it is relegated to a secondary effect. For the same reason higher spherical harmonics are neglected and the shape of the bubbles is taken to remain spherical. Therefore, the potential part of the flow is assumed to be dominated by radial oscillations, treating the translational part as vortical and lower order compared to the potential part, $|\boldsymbol{U}_v^*| \ll |\boldsymbol{U}_p^*|$.

2.1. *Radial motion*

As a first step, and following Landau & Lifshitz (1959), the dimensional velocity field is decomposed into an irrotational, $\boldsymbol{U}_p^*$ and a rotational or vortical part, $\boldsymbol{U}_v^*$. The former is described in terms of a scalar potential and the latter through a vector potential,

$$\boldsymbol{u}^* = \boldsymbol{U}_p^* + \boldsymbol{U}_v^*, \quad \boldsymbol{U}_p^* = \nabla \Phi^*, \quad \boldsymbol{U}_v^* = \nabla \times \boldsymbol{\Psi}^*. \tag{2.8a,b,c}$$

The pressure field is also decomposed in a fashion similar to the velocity field,

$$P^* = P_p^* + P_v^*. \tag{2.9}$$

The radial part of the flow exhibits very large velocities, especially for the large values of sound amplitude ε that give rise to acoustic streamers, which allows viscous effects in the bulk of the fluid to be neglected and the velocity potential to be introduced. For the same reason inclusion of compressibility is required in the model describing radial motion in the far field. When the Mach number of the flow, based on the radial velocity of the two bubbles, $\dot{R}_i^*$, is not very large, the far field flow is compressible and described by the wave equation whereas near the bubble–host fluid interface the flow field can be described by the Laplace equation, to leading order (Prosperetti & Lezzi 1986). This structure essentially leads to the Keller–Miksis (1980) model describing very fast radial oscillations of a bubble. The potential part of the flow is governed by the Laplace and Bernoulli equations, corresponding to the scalar potential, Φ^*, and the pressure field, respectively, coupled with the kinematic boundary condition at each bubble's surface, which is used in order to describe the instantaneous radial position of the interface.

$$\nabla^2 \Phi^* = 0, \tag{2.10}$$

$$P_p^* = P_{st}^* + \varepsilon P_{st}^* \sin(\omega_f t^*) - \rho \left(\frac{\partial \Phi^*}{\partial t^*} + \frac{1}{2} \frac{\partial {\Phi^*}^2}{\partial r^*} \right), \tag{2.11}$$

$$\nabla \Phi^* \cdot \boldsymbol{e}_{ri} = \dot{R}_i^*. \tag{2.12}$$

In (2.12) only the radial part of the interfacial velocity, J_i, in (2.4), has been included; $\boldsymbol{e}_{ri}$ denotes the unit vector in the radial direction of each bubble while dotted variables signify time derivatives. Due to the linearity of the Laplacian operator, quantities characterizing the potential part of the flow are given, in the vicinity of each bubble's interface, through a decomposition of the total velocity potential into two components, Φ_i^*, each representing the contribution from one of the two bubbles,

$$\Phi_i^* = -\frac{\dot{R}_i^*(t) R_i^{*2}(t)}{r_i^*}, \quad i = 1, 2. \tag{2.13}$$

In the above r_i^* denotes the radial coordinate of the local spherical coordinate system based on the centre of bubble i. It should be noted that when evaluated on each bubble's interface with the surrounding medium the contribution to the velocity potential from the opposite bubble becomes very small, $O((R_{i0}/L_0)^2)$. Then the potential part of the pressure becomes

$$P_p^* = P_{st}^* + \varepsilon P_{st}^* \sin(\omega_f t^*) + P_{p1}^* + P_{p2}^*, \tag{2.14}$$

with

$$P_{p1}^* + P_{p2}^*\big|_{r_i^*=R_i^*} = -\rho \left[\frac{\partial \Phi_i^*}{\partial t^*} + \frac{1}{2}\left(\frac{\partial \Phi_i^*}{\partial r^*}\right)^2 \Bigg|_{r_i^*=R_i^*} + \frac{\partial \Phi_{3-i}^*}{\partial t^*}\Bigg|_{r_{3-i}=L} \right], \tag{2.15}$$

where we have only kept terms up to $O(R_{i0}/L_0)$, i.e. the last term on the right-hand side of (2.15) which, essentially, represents bubble–bubble interaction.

Then the equation describing the evolution of the bubble radii with time is obtained by applying the normal force balance and the Bernoulli equation on the bubble surface and evaluating the pressure on it as predicted by the wave equation in the far field. It is in dimensionless form

$$\begin{aligned}
&\left[(1 - M\dot{R}_i)R_i\ddot{R}_i + \frac{4M}{Re}\ddot{R}_i + \left(\frac{3}{2} - \frac{M\dot{R}_i}{2}\right)\dot{R}_i^2\right] + \frac{1}{D}\left(\ddot{R}_{3-i}R_{3-i}^2 + 2R_{3-i}\dot{R}_{3-i}^2\right) \\
&\quad = (1 + M\dot{R}_i)\left[-P_{st} + P_u - \varepsilon P_{st}\sin t - \frac{4}{Re}\frac{\dot{R}_i}{R_i} - \frac{2}{We}\frac{1}{R_i}\right. \\
&\qquad \left. + \left(P_{st} - P_u + \frac{2}{We}\frac{R_{20}}{R_{i0}}\right)\frac{1}{R_i^{3\gamma}}\left(\frac{R_{i0}}{R_{20}}\right)^{3\gamma}\right] + M\left[-\varepsilon P_\infty R_i \cos t + \frac{4}{Re}\frac{\dot{R}_i^2}{R_i} + \frac{2}{We}\frac{\dot{R}_i}{R_i}\right. \\
&\qquad \left. + \left(P_{st} - P_u + \frac{2}{We}\frac{R_{20}}{R_{i0}}\right)\frac{\dot{R}_i}{R_i^{3\gamma}}\left(\frac{R_{i0}}{R_{20}}\right)^{3\gamma}\right],
\end{aligned} \tag{2.16}$$

$$R_1(t=0) = R_{10}/R_{20}, \quad R_2(t=0) = 1, \quad \dot{R}_i(t=0) = 0, \quad i = 1, 2. \tag{2.17}$$

In the above, the equilibrium radius of the right-hand bubble, R_{20}, and the inverse of the forcing frequency, $1/\omega_f$, are used as characteristic scales for space and time and $i = 1, 2$ for the left- and right-hand bubble respectively. P_{st}, P_u denote dimensionless pressure at steady state and the vapour pressure of the host fluid, respectively, the latter taken to be negligible for the purposes of the present study. They are both scaled with $\rho R_{20}^2 \omega_f^2$. Also, $Re = \rho R_{20}^2 \omega_f / \mu$, $We^{-1} = \sigma/(\rho R_{20}^3 \omega_f^2)$ and $M = R_{20}\omega_f / C$ denote the Reynolds, Weber and Mach numbers respectively, D is the instantaneous dimensionless distance between the centres of mass of the two bubbles, while γ is the adiabatic constant, taken to be 1.4 for an air bubble. It should be noted that (2.16) contains an $O(\dot{R}_{i0}/C \propto M)$ correction term for compressibility effects as suggested by Prosperetti & Lezzi; C, M, denote the speed of sound in the surrounding medium and the Mach number, respectively, and L_0, D_0, the dimensional and dimensionless initial distance between the two bubbles, respectively. This is also the model used by Mettin *et al.* (1997) for capturing the radial motion of two interacting bubbles. Equation (2.16) is solved simultaneously for the position of the two interfaces as well as the radial velocities and is subsequently used as input for the translational motion of each bubble.

2.2. *Translational motion*

The velocity field due to the translational part of the motion is much weaker, because $D \gg R_i$. Consequently, upon substituting (2.9) in the equation of motion, (2.1), with the incompressible form of the stress tensor,

$$T^*_{kl} = \mu \left(\frac{\partial u^*_k}{\partial x^*_l} + \frac{\partial u^*_l}{\partial x^*_k} \right), \tag{2.18}$$

we obtain the following dimensionless equation governing the vortical part of the flow:

$$\frac{\partial \boldsymbol{U}_v}{\partial t} + (\boldsymbol{U}_p \cdot \nabla)\boldsymbol{U}_v + (\boldsymbol{U}_v \cdot \nabla)\,\boldsymbol{U}_p = \frac{1}{Re}\Delta \boldsymbol{U}_v - \frac{\nabla P_v}{Re}, \tag{2.19}$$

where the term $(\boldsymbol{U}_v \cdot \nabla)\boldsymbol{U}_v$ has been dropped since the radial part of the motion is much larger than the translational part, and $\boldsymbol{U}^*_v$ has been made dimensionless via S which is a measure of the translational velocity of the two bubbles. As will be seen in the following S is set to be $(R_{20}\omega_f)(R_{20}/L_0)^2$. Similarly P^*_v is scaled with $(\mu S)/R_{20}$. Upon further manipulation of (2.19) and taking advantage of its linearity with respect to $\boldsymbol{U}_v$, it can be applied in the vicinity of each interface, taking the form

$$\frac{\partial \boldsymbol{U}_{vi}}{\partial t} + \nabla(\boldsymbol{U}_{pi} \cdot \boldsymbol{U}_{vi}) - \boldsymbol{U}_{pi} \times (\nabla \times \boldsymbol{U}_{vi}) = \frac{1}{Re}\Delta \boldsymbol{U}_{vi} - \frac{\nabla P_{vi}}{Re}. \tag{2.20}$$

In addition, the partial derivative $\partial \boldsymbol{U}_{vi}/\partial t$ can be taken with respect to a moving coordinate system that follows the instantaneous location of the centre of mass of each bubble without any loss in accuracy since

$$\left.\frac{\partial \boldsymbol{U}_{vi}}{\partial t}\right|_{fixed} = \left.\frac{\partial \boldsymbol{U}_{vi}}{\partial t}\right|_{moving} - \frac{S}{R_{20}\omega_f}(\boldsymbol{U}_i \cdot \nabla)\boldsymbol{U}_{vi}, \tag{2.21}$$

and $\boldsymbol{U}_i$ is the translational velocity of the centre of mass of each bubble which is scaled via S also. Clearly then the second term on the right-hand side of (2.21) can be dropped since $S/(R_{20}\omega_f) = (R_{20}/L_0)^2$, which is taken to be a small quantity in our analysis. In this moving coordinate system and near the bubble–liquid interface the radial part of the velocity becomes, $\boldsymbol{U}_{pi} = \nabla \Phi_i = (\dot{R}_i(t)R_i^2(t)/r_i^2)\boldsymbol{e}_{ri}$, with r_i, $\boldsymbol{e}_{ri}$, θ_i, $e_{\theta i}$, ϕ_i, $\boldsymbol{e}_{\phi i}$, representing the radial, meridional and azimuthal coordinates and unit vectors of the coordinate system that moves with the ith bubble. It can then be easily seen that, in view of the axial symmetry of the problem and the spherical shape of the bubbles,

$$\boldsymbol{U}_{vi} = \nabla \times \boldsymbol{\Psi}_i = \frac{2}{r_i} f_i \cos\theta_i \boldsymbol{e}_{ri} - \left(\frac{\partial f_i}{\partial r_i} + \frac{1}{r_i} f_i \right) \sin\theta_i \boldsymbol{e}_{\theta i}, \quad \boldsymbol{\Psi}_i = f_i(r_i, t)\sin\theta_i \boldsymbol{e}_{\phi i} \tag{2.22}$$

and consequently, after substituting in (2.20) and integrating,

$$P_v = -\cos\theta \left[r\frac{\partial^2 f_i}{\partial r \partial t} + \frac{\partial f_i}{\partial t} + \frac{\dot{R}R^2}{r}\left(\frac{2f_i'}{r} + f_i'' \right) + \frac{1}{Re}\left(-f_i''' r - 3f_i'' + \frac{2f_i'}{r} - \frac{2f_i}{r^2} \right) \right], \tag{2.23}$$

whereas taking the curl of (2.20) we find

$$\frac{\partial G_i}{\partial t} + \frac{\dot{R}R^2}{r^2}\left(G_i' - \frac{1}{r}G_i \right) = \frac{1}{Re}\left(G_i'' + \frac{2}{r}G_i' - \frac{2}{r^2}G_i \right), \quad G_i = f_i'' + \frac{2f_i'}{r} - \frac{2f}{r^2}, \tag{2.24}$$

with G_i representing the vorticity, $\boldsymbol{\Omega}_i$, generated by the motion of bubble i, since

$$\boldsymbol{\Omega}_i = \nabla \times \boldsymbol{U}_{vi} = -\Delta \boldsymbol{\Psi}_i = -G_i \sin\theta \boldsymbol{e}_\phi. \tag{2.25}$$

In the above, primes denote differentiation with respect to r. The vortical flow field should also satisfy the following boundary conditions:
zero vortical velocity and vorticity in the far field,

$$\frac{\partial f_i}{\partial r_i}(t, r \to \infty), \quad G_i(t, r \to \infty) \to 0, \tag{2.26}$$

continuity of normal velocity at the interface $r = R_i(t)$,

$$\left(\nabla \Phi_1^* + \nabla \Phi_2^* + \boldsymbol{U}_{v1}^* + \boldsymbol{U}_{v2}^*\right) \cdot \boldsymbol{n}_i = \boldsymbol{U}_i^* \cdot \boldsymbol{n}_i + \dot{R}_i^*, \tag{2.27}$$

or, after introducing dimensionless variables and retaining terms of $O((R_{20}/L_0)^2)$,

$$f_i = \frac{R_i U_i}{2} \pm \frac{R_i \dot{R}_{3-i} R_{3-i}^2}{2} \left(\frac{D_0}{D}\right)^2 \tag{2.28}$$

(where the plus and minus signs correspond to the left- and right-hand bubble respectively),
and zero tangential stress at the interface $r = R_i$(t),

$$f_i'' = 0. \tag{2.29}$$

Finally, the normal force balance on each of the two bubbles has to be satisfied. It is used in order to calculate the translational velocities of the two bubbles, and is written in dimensionless form as follows:

$$P_{gi} + P_u - P_p - \frac{S}{R_{20}\omega_f} P_v = \frac{1}{We} \nabla \cdot \boldsymbol{n}_i + -\frac{2}{Re} \boldsymbol{n}_i \cdot \boldsymbol{T} \cdot \boldsymbol{n}_i. \tag{2.30}$$

In (2.30), $P_{gi} = P_{gi}^*/(\rho R_{20}^2 \omega_f^2)$ denotes the dimensionless pressure inside bubble i, the gas inside the bubbles is treated as inviscid with uniform pressure, and $\boldsymbol{T}$ represents the dimensionless incompressible deviatoric stress in the fluid (2.18). As was shown in the beginning of § 2.1, all the terms in (2.30) have been accounted for in the radial part of the motion up to $O(R_{20}/L)$ (see also (2.15)). Introducing the flow decomposition into radial and vortical parts in equation (2.30), transforming the partial derivative of the velocity potential with respect to time so that it is evaluated in a spherical coordinate system attached to the ith bubble,

$$\left.\frac{\partial \Phi_i}{\partial t}\right|_{fixed} = \left.\frac{\partial \Phi_i}{\partial t}\right|_{moving} - \frac{S}{R_{20}\omega_f} (\boldsymbol{U}_i \cdot \nabla) \Phi_i, \tag{2.31}$$

and retaining terms of order $(R_{20}/L_0)^2$ in the part of pressure associated with potential flow, P_p, we obtain

$$P_p(r = R_i) = O(1) + O\left(\frac{R_{20}}{L_0}\right) + \frac{S}{R_{20}\omega_f} U_i \dot{R}_i \cos\theta_i \pm \left(\frac{R_{20}}{L_0}\right)^2 D_0^2 \cos\theta_i \frac{\mathrm{d}}{\mathrm{d}t}\left(\frac{R_i \dot{R}_{3-i} R_{3-i}^2}{D^2}\right) + o\left(\frac{R_{20}}{L_0}\right)^2. \tag{2.32}$$

Substituting (2.32) along with the vortical parts of the pressure and velocity fields, which also scale like $S/(R_{20}\omega)$, in (2.30) we note first that in order for all these terms to

balance, the characteristic translational velocity, S, has to scale like $(R_{20}\omega)(R_{20}/L_0)^2$, and second that the translational velocity U_i is given by the following equation, evaluated at the interface $r_i = R_i(t)$:

$$-U_i\dot{R}_i + R_i\frac{\partial^2 f_i}{\partial r_i \partial t} + \frac{\partial f_i}{\partial t} + \dot{R}_i R_i\left(2\frac{f_i}{R_i} + f_i''\right) + \frac{1}{Re}\left(\frac{6f_i'}{R_i} - \frac{6f_i}{R_i^2} - 3f_i'' - R_i f_i'''\right) = \pm D_0^2\frac{\mathrm{d}}{\mathrm{d}t}\left(\frac{R_i\dot{R}_{3-i}R_{3-i}^2}{D^2}\right), \quad (2.32)$$

with the plus or minus sign on the right-hand-side of this equality signifying the left- and right-hand bubble, respectively. Finally the time derivative of the distance between the centres of mass of the two bubbles is obtained via the difference between their translational velocities,

$$\frac{\mathrm{d}D}{\mathrm{d}t} = \frac{U_2 - U_1}{D_0^2}. \quad (2.33)$$

3. Numerical solution

The radial part of the motion is solved numerically via the explicit fourth-order Runge–Kutta method. At each time step four unknown variables are updated simultaneously, namely the radial position and its time derivative for each of the two interfaces. Due to the large values of the sound amplitude, ε, the radial velocities of the two bubbles can be very large, thus requiring very small values of the time step in order to capture the dynamics of the motion. In fact, when ε approaches the Blake threshold, $\varepsilon \sim 1.3$, dimensionless time steps as small as 10^{-6} were required for an accurate solution. During certain time intervals for which radial velocity attained its maximum value even lower time steps were necessary. The dimensionless period of the main oscillatory motion that is induced by the external forcing is $T = T_f/(1/\omega_f) = (2\pi/\omega_f)/(1/\omega_f) = 2\pi$, making a time-step of $\Delta t = 0.001$ sufficiently small and the most commonly used one in the present study. Occasionally, and in order to reduce computational time in cases exhibiting intense variation of the radial motion, a time adaptation technique has been implemented that utilizes time-step halving for calculating the solution at a certain time instant. Usually, however, a constant time step was used.

The translational part of the motion involves solving for the vorticity of the flow, G_i, for each bubble. Given the variation of the location of the bubble wall, discretization of the domain is facilitated significantly if it is mapped on a fixed domain via the transformation $\eta = r/R(t)$. This introduces the radial position and its derivative in more parts of the problem formulation but it simplifies the numerical solution. Another important aspect of the vortical motion is the treatment of the stream function, f, and vorticity, G. In order to lower the order of the derivatives that appear in the problem we utilize the definition of G, (2.24), along with boundary conditions (2.26)–(2.28) in order to express f as a function of G. Thus we obtain

$$f_i = \frac{r_i}{3}\left[\int_{R_i}^{r_i} G_i\,\mathrm{d}s_i - \int_{R_i}^{\infty} G_i\,\mathrm{d}r_i\right] + \frac{R_i^3}{3r_i^2}\left[\int_{R_i}^{\infty} G_i\,\mathrm{d}r_i - \int_{R_i}^{r_i}\frac{s_i^3}{R_i^3}G_i\,\mathrm{d}s_i\right] + \frac{R_i^3 U_i}{2r_i^2} \pm \frac{R_i^3 R_{3-i}^2\dot{R}_{3-i}}{2r_i^2}\left(\frac{D_0}{D}\right)^2, \quad (3.1)$$

where the plus and minus signs signify the left- and right-hand bubble, respectively. Upon introduction of the transformation for the radial coordinate given above the problem formulation becomes

$$\frac{\partial G_i}{\partial t} = \frac{\dot{R}_i}{R_i}\left[\frac{\partial G_i}{\partial \eta_i}\left(\eta_i - \frac{1}{\eta_i^2}\right) + \frac{G_i}{\eta_i^3}\right] + \frac{1}{Re}\frac{1}{R_i^2}\left[\frac{\partial^2 G_i}{\partial \eta_i^2} + \frac{2}{\eta_i}\frac{\partial G_i}{\partial \eta_i} - \frac{2G_i}{\eta_i^2}\right], \tag{3.2}$$

$$\eta_i \to \infty, \quad G_i \to 0, \quad t = 0, \quad G_i = 0, \tag{3.3}$$

$$\eta_i = 1, \quad G_i + 2\int_1^\infty G_i \mathrm{d}\eta_i + \frac{3U_i}{R_i} \pm \frac{3R_{3-i}^2 \dot{R}_{3-i}}{R_i}\left(\frac{D_0}{D}\right)^2 = 0, \tag{3.4}$$

$$\eta_i = 1, \quad -R_i^2 \int_1^\infty \frac{\partial G_i}{\partial t}\,\mathrm{d}\eta_i - \frac{R_i}{2}\dot{U}_i = \int_1^\infty 2R_i\dot{R}_i G_i\,\mathrm{d}\eta_i + \frac{1}{Re}\left(-G_i + \frac{\partial G_i}{\partial \eta_i}\right) + \frac{3\dot{R}_i}{2}U_i \pm \frac{3D_0^2}{2}\frac{\mathrm{d}}{\mathrm{d}t}\left(\frac{R_i R_{3-i}^2 \dot{R}_{3-i}}{D^2}\right), \tag{3.5}$$

$$\frac{\mathrm{d}D}{\mathrm{d}t} = \frac{U_2 - U_1}{D_0^2}. \tag{3.6}$$

Solution of equations (3.2)–(3.6) requires discretization in time as well as in the radial direction. Since the radial motion of the two bubbles is used as input in the above set of equations the two problems are solved simultaneously. The fourth-order Runge–Kutta method is used for integrating in time in conjunction with the finite element method, with B-cubic splines as basis functions, for discretization in the radial direction. More details on the combined implementation of these two methods in describing bubble dynamics can be found in Pelekasis, Tsamopoulos & Manolis (1992). The time step was determined by the radial motion with the understanding that, in general, the translational motion required smaller time steps due to the simultaneous spatial and temporal discretization, especially for large values of the disturbance amplitude, $\varepsilon \sim 1$. For the spatial discretization, 15–20 elements were enough for capturing the vorticity variation in the liquid phase. Special care had to be taken as the Reynolds number increased, in which case a vorticity boundary layer was generated near the bubble walls, and packing of the elements was employed in order to improve accuracy in that region.

This procedure is employed in calculating the instantaneous translational velocity of the left-hand bubble for different time and space discretization levels. A pair of bubbles with equilibrium radii $R_{10} = 10\,\mu\mathrm{m}$ and $R_{20} = 9\,\mu\mathrm{m}$ is used; index one-hand indicates the left bubble. The forcing frequency is $\omega_f/2\pi = 175\,\mathrm{kHz} \approx 0.51\omega_{10}$, while two different values for the amplitude of the disturbance, 0.25 and 0.5, are tested. Discrepancies in the evolution of the instantaneous translational velocity, calculated using 20 and 40 elements with time step $\Delta t = 2 \times 10^{-4}$ and 0.5×10^{-4} respectively, are almost indistinguishable. The time step has to be decreased as the number of elements increases in order to maintain numerical stability. In the above tests the inter-bubble distance was set to 1 mm and was assumed to remain constant throughout the simulation, which means that (3.6) is not utilized. It should also be pointed out that excluding (3.6) from the numerical formulation reduces the numerical effort significantly since it decouples the solution of the translational part of the motion of each bubble (equations (3.2)–(3.5)). This assumption does not restrict the validity of the results presented here since, for small and moderate sound amplitudes and for

relatively short periods of time, the distance travelled by the centres of mass of the two bubbles is negligible compared with their initial distance apart.

In the present study, in addition to the type of simulations described in the previous paragraph, a number of numerical simulations were also carried out that allow for the variation of the instantaneous distance between the two centres of mass for long periods of time. This requires incorporating (3.6) in the model governing the translational part of the motion. Thus the translational and radial velocities of the two bubbles are calculated simultaneously with the instantaneous distance between their centres of mass. It should be stressed that, in order to avoid a very intense numerical effort whenever (3.6) is included, the translational part of the motion is simplified to its asymptotic form, valid for large Re. Thus, such simulations only require solution of five ODE's: (2.16) and (4.19) for each of the two bubbles along with (3.6). Equation (4.19) describing the translational velocity of each bubble will be given in the following section.

In this fashion, the motion is followed for a specified amount of time and a certain sound amplitude, and the dynamics of the binary bubble system is determined for a range of values of the two equilibrium radii, R_{10} and R_{20}, depending on the evolution of the inter-bubble distance, $\langle D \rangle$, averaged over the period of the forcing. More specifically, when $\langle D \rangle$ increases as time increases a case of bubble repulsion is registered. On the other hand, when $\langle D \rangle$ decreases or when it becomes smaller than a lower threshold value, e.g. $3(R_{10} + R_{20})$, a case of bubble attraction or coalescence is registered. Clearly the latter case needs further investigation since the validity of our model becomes questionable in this range of distances. Finally, when $\langle D \rangle$ remains constant or oscillates within a well defined range of values we have the situation of a stable pair of bubbles which conforms with experimental observations of acoustic streamers. This approach is an extension of the study by Barbat *et al.* (1999), since it includes the effect of viscous dissipation and strong nonlinearity. The classification of binary bubble systems outlined above is very similar to the one presented in Barbat *et al.* with the understanding that, owing to the effect of viscous damping, in the cases for which they predict stable oscillations of $\langle D \rangle$, in the present study $\langle D \rangle$ tends to a constant value. Specific cases are presented in the following sections.

4. Asymptotic solution in the limit $Re \gg 1$

The formulation of the translational part of the motion, as given by (3.2)–(3.6), is a linear problem with the radial motion of the two bubbles used as input and Re, based on the characteristics of the radial motion, as a parameter. As a first step towards evaluating the effect of viscosity on the translational motion of the two bubbles one would first have to obtain the $O(1/Re)$ correction to the inviscid prediction for the secondary Bjerknes force as given by the following equation:

$$\dot{U}^* = 3\dot{W}^* - (U^* - W^*)\frac{\dot{M}^*}{M^*} \tag{4.1}$$

where U^* denotes the dimensional translational velocity of a bubble immersed in a fluid which, in the absence of the bubble, would have had an acceleration $\dot{W}^*$, and $M^* = \frac{4}{3}\pi\rho R^{*3}$ denotes the liquid mass displaced by the bubble. The above equation originates from equation 6.8.24 in Batchelor (1967) when the displaced mass is taken to be much larger than the mass of the bubble itself, as is normally the case for gas bubbles, see also Pozrikidis (1997). Mettin *et al.* (1997) have essentially used the time-averaged version of (4.1) over one period of the forcing, denoted by angular brackets

$\langle\,\rangle$, in order to calculate the Bjerknes force between the two bubbles (equation 6.8.25 in Batchelor),

$$\boldsymbol{F}_B = \langle \boldsymbol{F}_{12} \rangle \propto -\frac{\rho}{4\pi L_0^2} \left\langle \dot{V}_1^* \dot{V}_2^* \right\rangle \boldsymbol{e}_z, \tag{4.2}$$

where L_0 is a measure of the distance between the two bubbles, ρ is the density of the fluid in which they are immersed, V_1^*, V_2^*, denote the dimensional volumes of the left- and right-hand bubbles, respectively, and $\boldsymbol{e}_z$ denotes the vector connecting the two centres of mass of the two bubbles with its positive direction pointing from the left- to the right-hand bubble (see also figure 2). This formula can be obtained from (4.1) when two bubbles, located at a distance apart much larger than their radii, undergo spherosymmetric oscillations. In the following we will recover (4.1), in the limit as $Re \to \infty$, in the context of our study and provide the $O(1/Re)$ correction to it which, in view of the dynamic nature of the motion, will be valid up to $t = O(1)$.

It should be pointed out that resorting to an asymptotic solution in the limit as $Re_T \to \infty$, the Reynolds number based on the characteristic translational velocity S, would not be very helpful because that would require very large values of S. This requirement, however, would tend to violate an essential assumption of our analysis, and of the analysis used by Mettin *et al.* (1997), Oguz & Prosperetti and Crum (1975), namely that the translational motion of the two bubbles be a secondary effect compared to their radial motion. More specifically, $Re = \rho\omega_f R_{20}^2/\mu \gg 1$ is a much less restrictive requirement than $Re_T = \rho S R_{20}/\mu \gg 1$ in view of the fact that $S \ll R_{20}\omega_f$ for the problem formulation in §§2.1, 2.2 to be valid. Large values of Re_T can only be obtained in the context of the present problem if S becomes very large, which essentially requires very large values of ε. Then, as will be seen in the following section, the instantaneous translational velocity will start to grow faster than the radial velocity until they become comparable in size, thus rendering the validity of the problem formulation questionable. Moreover, asymptotic expansions just in inverse powers of Re cannot be valid for all times, because of the growing vorticity layer on the surface of each bubble. Consequently, we follow a different approach and carry out an expansion in time of the quantities describing the translational part of the motion, given the solution to the radial part. To this end, upon introducing the transformation,

$$\tau = \frac{t}{Re}, \tag{4.3}$$

in the time derivatives concerning one of the two bubbles, for example the left-hand one,

$$\left.\frac{\partial G}{\partial \tau}\right|_\eta \frac{1}{Re} = \left.\frac{\partial G}{\partial t}\right|_\eta, \quad \frac{\mathrm{d}R}{\mathrm{d}\tau}\frac{1}{Re} = \dot{R}, \tag{4.4}$$

and setting

$$-\frac{R_2^{*2}\dot{R}_2^*}{L^2}\boldsymbol{e}_z = -W\frac{R_{20}^3\omega_f}{L_0^2}\boldsymbol{e}_z = W^*\boldsymbol{e}_z \quad \left(W = \dot{R}_2 R_2^2 \frac{D_0^2}{D^2}\right), \tag{4.5}$$

as the translational velocity induced by the radial oscillations of the right-hand bubble at the location of the left-hand one, we eliminate Re from the formulation of the translational part of the motion. Then, noting that the translational part of the problem formulation is essentially one of vorticity diffusion from the bubble surface towards the bulk of the host fluid where vorticity is zero, and in analogy with similar problems in planar geometry, we introduce the following transformation of the radial

coordinate:

$$\frac{\eta-1}{\sqrt{\tau}}=\zeta, \tag{4.6}$$

where ζ is a similarity-type variable that extends from zero on the surface of the two bubbles to infinity in the bulk of the host liquid. The square root of transformed time τ is used to account for the $O(Re^{-1/2})$ boundary layer that is formed near the interface. In this fashion (3.2)–(3.5) become, for the left-hand bubble,

$$\frac{\partial G}{\partial \tau}-\frac{\partial G}{\partial \zeta}\frac{\zeta}{2\tau}=\frac{\mathrm{d}R}{\mathrm{d}\tau}\frac{1}{R}\left[\frac{\partial G}{\partial \zeta}\frac{1}{\sqrt{\tau}}\frac{3\zeta\sqrt{\tau}+3\zeta^2\tau+\zeta^3\tau^{3/2}}{1+2\zeta\sqrt{\tau}+\zeta^2\tau}+\frac{G}{(\zeta\sqrt{\tau}+1)^3}\right] + \frac{1}{R^2}\left[\frac{1}{\tau}\frac{\partial^2 G}{\partial \zeta^2}+\frac{2}{\zeta\sqrt{\tau}+1}\frac{\partial G}{\partial \zeta}\frac{1}{\sqrt{\tau}}-\frac{2G}{(\zeta\sqrt{\tau}+1)^2}\right], \tag{4.7}$$

$$\zeta\to\infty, \quad G\to 0, \quad \tau=0, \quad G=0, \tag{4.8}$$

$$\zeta=0, \quad G(\zeta=0)=-2\int_0^\infty G\sqrt{\tau}\,\mathrm{d}\zeta-3\frac{U}{R}-3\frac{W}{R}, \tag{4.9}$$

$$\zeta=0, \quad -\frac{3}{2}D_0^2\left(W\frac{\mathrm{d}R}{\mathrm{d}\tau}+R\frac{\mathrm{d}W}{\mathrm{d}\tau}\right)-\frac{R}{2}\frac{\mathrm{d}U}{\mathrm{d}\tau}-\frac{3}{2}U\frac{\mathrm{d}R}{\mathrm{d}\tau} = R^2\int_0^\infty\left(\frac{\partial G}{\partial \tau}-\frac{\partial G}{\partial \zeta}\frac{\zeta}{2\tau}\right)\sqrt{\tau}\,d\zeta+2R\frac{\mathrm{d}R}{\mathrm{d}\tau}\int_0^\infty G\sqrt{\tau}\,\mathrm{d}\zeta+\frac{\partial G}{\partial \zeta}\frac{1}{\sqrt{\tau}}-G. \tag{4.10}$$

In the above equations $\mathrm{d}R/\mathrm{d}\tau$ and U denote the instantaneous radial and translational velocities of the left-hand bubble and G the vorticity in the vicinity of the left-hand bubble. The formulation for the right-hand bubble is the same with the exception of the sign in front of the terms involving W, which will be positive with W defined in terms of the radial motion of the left-hand bubble.

We now look for a solution of the problem defined by (4.7)–(4.10) in terms of the vorticity and the translational velocity of the left-hand bubble, as an expansion in time of the form

$$G(\zeta,\tau)=G_0(\zeta)+\sqrt{\tau}G_1(\zeta)+\tau G_2+O(\tau^{3/2}), \tag{4.11}$$

$$U(\tau)=U_0+\sqrt{\tau}U_1+\tau U_2+O(\tau^{3/2}). \tag{4.12}$$

Clearly then, and in view of (4.3), the above equations can also be considered as expansions in powers of $Re^{-1/2}$ that are valid in the limit $Re\to\infty$, provided time t remains an $O(1)$ quantity. Due to the simultaneous variation of R and W one would need, in general, to carry out a simultaneous expansion in τ, or $Re^{-1/2}$, of the radial motion as well. For convenience we will proceed with the expansion in time τ, keeping in mind that we are interested in the leading-order correction to (4.1).

Introducing (4.11) and (4.12) in (4.7)–(4.10) we obtain, for the vorticity equation,

$$\tau^{-1}: \quad \frac{\partial^2 G_0}{\partial \zeta^2}+\frac{\zeta R^2}{2}\frac{\partial G_0}{\partial \zeta}=0, \tag{4.13}$$

$$\tau^{-1/2}: \quad \frac{R^2\zeta}{2}\frac{\partial G_1}{\partial \zeta}+\frac{\partial^2 G_1}{\partial \zeta^2}+2\frac{\partial G_0}{\partial \zeta}=0, \tag{4.14}$$

for the boundary condition for the fluid velocity at the bubble–host fluid interface,

$$\begin{array}{ll} \tau^0: & G_0(\zeta=0) = -\frac{3}{R}(U_0+W) \\ \vdots & \end{array}, \tag{4.15}$$

and for the normal force balance at the bubble–host fluid interface,

$$\tau^{-1/2}: \quad \int_0^\infty R^2 \frac{\partial G_0}{\partial \zeta}\frac{\zeta}{2}\mathrm{d}\zeta - \left.\frac{\partial G_0}{\partial \zeta}\right|_{\zeta=0} = 0, \tag{4.16}$$

$$\tau^0: \quad \int_0^\infty R^2 \frac{\partial G_1}{\partial \zeta}\frac{\zeta}{2}\mathrm{d}\zeta - \frac{R}{2}\frac{\mathrm{d}U}{\mathrm{d}\tau} = \frac{3}{2}U\frac{\mathrm{d}R}{\mathrm{d}\tau} + \left.\frac{\partial G_1}{\partial \zeta}\right|_{\zeta=0} - G_0(\zeta=0) + \frac{3}{2}\left(W\frac{\mathrm{d}U}{\mathrm{d}\tau} + R\frac{\mathrm{d}W}{\mathrm{d}\tau}\right).$$

$$\vdots \tag{4.17}$$

Equation (4.16) is trivial and can be easily retrieved by integrating the $O(\tau^{-1})$ relation (4.13) that arises from the vorticity equation over the entire range of ζ values from zero to infinity. Therefore it does not contain any useful information. Next, integration of (4.14) with ζ varying from zero to infinity and introduction of the result, along with (4.15) in (4.17), gives

$$\frac{R}{2}\frac{\mathrm{d}U_0}{\mathrm{d}\tau} + \frac{3}{2}\frac{\mathrm{d}R}{\mathrm{d}\tau}U_0 + \frac{3}{2}\left(W\frac{\mathrm{d}R}{\mathrm{d}\tau} + R\frac{\mathrm{d}W}{\mathrm{d}\tau}\right) + \frac{9}{R}(U_0+W) = 0. \tag{4.18}$$

Lastly, reverting to the $t = Re\tau$ variable we obtain,

$$\dot{U}_0 + 3\frac{\dot{R}}{R}U_0 + \frac{3}{R}(W\dot{R} + R\dot{W}) + \frac{18}{ReR^2}(U_0+W) = 0, \tag{4.19}$$

which is valid to $O(Re^{-1})$ with an error of $O(Re^{-3/2})$. Clearly, the larger the values reached by Re the longer the time interval for which (4.19) is valid irrespective, in principle, of the intensity of sound ε. An interesting aspect of equation (4.19) is that it can also be obtained from (4.1), with the addition of the drag force as calculated by Levich's (1962) formula:

$$\boldsymbol{F}_D = 12\mu\pi R^* U_r^* \boldsymbol{e}_z, \tag{4.20}$$

where e_z is the direction of the motion, R^* the bubble radius and U_r^* the steady translational velocity of a bubble relative to the surrounding fluid; the dimensionless form of the latter is $U_r = U + W = U_r^*/S$, also scaled via S. Substituting (4.20) in (4.1) and non-dimensionalizing one obtains (4.19) for the translational velocity of the left-hand bubble. Magnaudet & Legendre (1998) also use this expression, which, upon converting to a coordinate system fixed in the bubble centre, reduces to equation (22*a*) in their article, in order to obtain the drag force on a spherical bubble with a time-dependent radius. They also point out that this formula is of wider validity than expected since it requires large values of the Reynolds number based on the radial velocity, rather than the translational one which is more restrictive. The present investigation provides a formal derivation of this formula in the context of a time-dependent motion, points out its limitations regarding the time interval over which it is used, $t = O(1)$ when Re is large, and sets the stage for obtaining higher-order corrections. The same type of solution in terms of the drag coefficient, as implied by (4.19), and the asymptotic behaviour of vorticity at small times for large Re, (4.11), was obtained in a slightly different context, namely a single bubble in a time-dependent

oncoming stream, by Slavchev & Simeonov (1979). It should also be pointed out that the approach presented above, i.e. expanding in ascending powers of $\tau^{1/2}$ or, equivalently, of $Re^{-1/2}$, is similar to the oscillatory problem solved by Fyrillas & Szeri (1994) in the context of mass transport across the interface of a spherical bubble undergoing volume oscillations. In that case the Péclet number controls the relative importance of diffusion and convection across the interface, instead of the Reynolds number controlling vorticity transport in the present study.

Crum (1975), in one of the first attempts to measure and calculate the drift velocity of two interacting bubbles in a stationary sound field, used Moore's (1963) $O(Re^{-3/2})$ correction to Levich's formula for a bubble rising with a large Re_T,

$$C_D = \frac{48}{Re_T}\left(1 - \frac{2.21}{(Re_T)^{1/2}} + \dots\right), \quad Re_T = \frac{2\rho U^* R^*}{\mu}, \tag{4.21}$$

with significant improvement over with the empirical expression provided by Haberman & Morton's (1953) measurements. It can be seen that introduction of the last term on the left-hand side of (4.19) works at least as well since it complies with the $1/L^2$ dependence on the distance between the bubbles for the attracting drift velocity of two bubbles cavitating below resonance. In addition, and provided that the appropriate amplitude, $\varepsilon \approx 0.985$, and frequency, $\omega_f/2\pi = 8.125\,\text{kHz}$, of the sound field are used on bubbles of similar size as those used in his experiments, $R_{10} = R_{20} \approx 0.053\,\text{cm}$, $L = 0.4\,\text{cm}$, the average dimensional drift velocity predicted by (4.19) is similar to that reported by Crum, $\langle U^* \rangle \approx 10\,\text{cm/s}^{-1}$. The asymptotic expression proposed here, however, is simpler to implement and has a wider range of validity since it does not require large values of Re_T.

5. Results and discussion

5.1. *Interaction of two relatively large bubbles, $R_{i0} \sim 100\,\mu m$*

We first examine the case of two air bubbles interacting in water, when their equilibrium radius is on the order of 100 μm, the forcing frequency of the acoustic disturbance is $\omega_f/2\pi = 16.8\,\text{kHz}$ and its amplitude ranges between 0.05 and 0.8. In this case Re based on the radial motion is $Re = 1055$ and the asymptotic theory is applicable for a significant time interval of the combined motion. This is the situation examined by Oguz & Prosperetti (1990) in an effort to explain the mechanism behind the formation of stable bubble clusters reported by Crum & Nordling (1972). This pattern was observed under conditions very similar to those prevailing in the experiments for which acoustic streamers are observed (Mettin *et al.* 2000), namely the bubbles are driven below resonance and at very high amplitude. It is therefore useful in the context of the present study to examine the validity of the mechanisms proposed by the above investigators. In particular, Oguz & Prosperetti examined the case of two bubbles whose distance apart along the centreline is 5 mm and equilibrium radii are $R_{10} = 100\,\mu\text{m}$ and $R_{20} = 90\,\mu\text{m}$, respectively. For air bubbles of this size oscillating in water at atmospheric pressure the linear resonance frequencies for volume oscillations are given by Minnaert's (1933) formula, corrected to include viscous effects due to the normal stress at the bubble's interface,

$$\omega_{i0} = \frac{1}{R_{i0}\sqrt{\rho}}\left[3\gamma\left(p_{st} + \frac{2\sigma}{R_{i0}}\right) - \frac{2\sigma}{R_{i0}} - \frac{4\mu^2}{\rho R_{i0}^2}\right]^{1/2}. \tag{5.1}$$

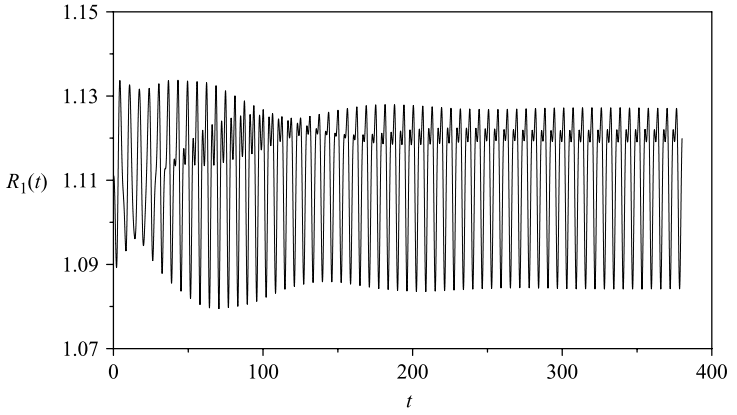

FIGURE 3. Evolution of the radial position of the left-hand bubble, $R_{10} = 100\,\mu\text{m}$, when $\varepsilon = 0.05$.

Thus, $\omega_{10}/2\pi = 33\,\text{kHz}$ and $\omega_{20}/2\pi = 36.5\,\text{kHz}$ and, since $\omega_f/2\pi = 16.8\,\text{kHz}$, they are driven below resonance with forcing frequency almost half their eigenfrequencies for volume oscillations. In this context, Oguz & Prosperetti found that, contrary to the classical Bjerknes theory for bubbles driven below resonance, the two bubbles do not always attract each other. Their behaviour depends on the level of nonlinearity, shifting from attraction to repulsion as ε increases from 0.1 to 0.5, as a result of the growth of the second harmonic, $2\omega_f$, of the forcing frequency due to nonlinear interaction. Thus, they conjectured that this mechanism might be responsible for the appearance of stable bubble clusters since it leads to a sign inversion of the secondary Bjerknes force and prevents coalescence. Doinikov (1999*b*) arrived at a similar result by considering the second harmonic component of the interaction force between two air bubbles with water as the host fluid.

We examine this pattern in the present study by both asymptotically and numerically solving the full equations. To this end, we examine the radial and translational motion of two bubbles with the same characteristics as those used by Oguz & Prosperetti, and fixed inter-bubble distance, $L = L_0 = 5\,\text{mm}$. Figure 3 shows the radial oscillations of the left-hand bubble, $R_{10} = 100\,\mu\text{m}$, when $\varepsilon = 0.05$. After an initial transient, the radial motion reaches a steady oscillatory state with dimensionless period 2π, with its dimensional counterpart determined by the forcing frequency. This is a result of the action of viscous damping on the radial motion of the bubble and the time needed to reach this type of motion is determined by *Re*. The instantaneous translational velocity of the same bubble is shown in figure 4, both as predicted by (4.19) and as calculated via numerical integration of (3.2)–(3.5), given the radial part of the motion. The two curves are almost identical at the beginning of the motion, with the asymptotic solution gradually underpredicting, on average, the translational velocity as time increases. The evolution of the translational velocity averaged over one dimensionless period in both cases is also shown in figure 5. Clearly, the translational motion follows the radial, in the sense that it tends to acquire a constant average drift velocity when the radial part of the motion reaches a steady periodic state. It is an attractive drift velocity, as expected by classical Bjerknes theory for bubbles driven below resonance. The existence of a drift velocity has been observed experimentally by Crum (1975) in his experiments with bubbles interacting in a stationary sound field. This is due to the effect of viscous damping on the translational motion of the

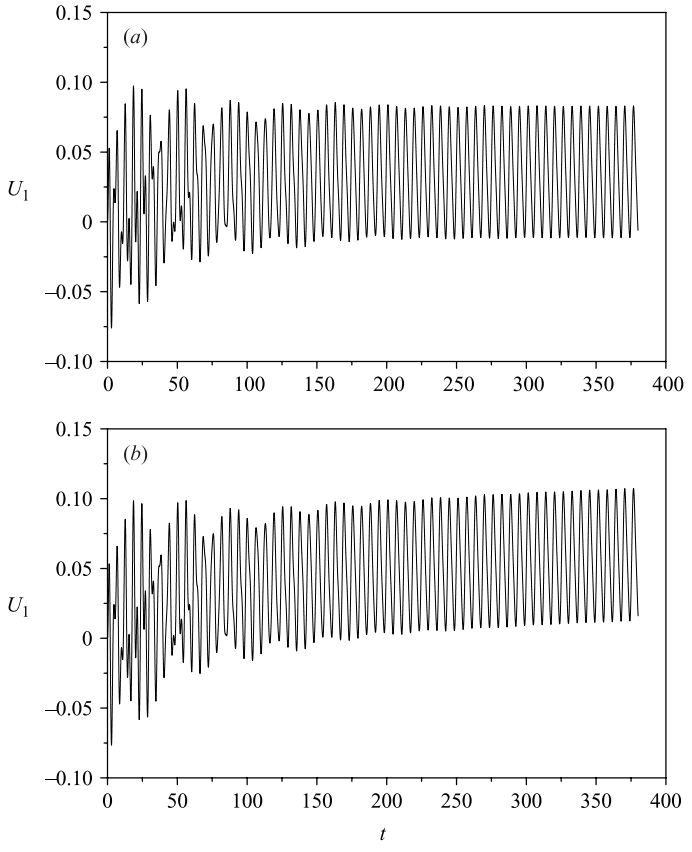

FIGURE 4. (*a*) Asymptotic and (*b*) numerical solution for the translational velocity of the left-hand bubble, $R_{10} = 100\,\mu\text{m}$, when $\varepsilon = 0.05$.

two bubbles and it is reminiscent of the 'Stokes terminal' velocity of bubbles rising or drops falling in viscous liquids.

The difference in the long-time behaviour of the average translational velocity as predicted by the numerical and asymptotic solutions is discussed next. Indeed this should have been expected in view of the fact that the latter solution was obtained in the limit as $\tau = t/Re \to 0$, whereas the former as $\tau \to \infty$ exhibits the $\sim\tau^{-1/2}$ behaviour common to many transient diffusive processes, as is the case in the present study due to the gradual thickening of the vorticity boundary layer (see also the discussion in Batchelor 1967). This is illustrated by the inset in figure 5, where the numerical solution and a fit of the $\tau^{-1/2}$ law are plotted as a function of the long time scale $\tau = t/Re$. Clearly the average translational velocity follows an $O(\tau^{-1/2})$ transient before it reaches the steady drift velocity. However, this is an asymptotic result typically obtained in the limit as $\tau \to \infty$ and cannot be captured by a small-τ analysis, such as the one leading to (4.19). Hence, (4.19) predicts an almost exponentially fast approach of the steady drift velocity rather than the $O(\tau^{-1/2})$ behaviour.

It should also be stressed that when the long-time behaviour of the translational motion of the bubbles is considered, inertia will start playing a central role in the dynamics, factor $(\mathrm{d}R/\mathrm{d}\tau)/R = (\dot{R}Re\,)/R$ in (4.7). Consequently, and in view of the fact that Re can be scaled out of the formulation for the translational part of the motion,

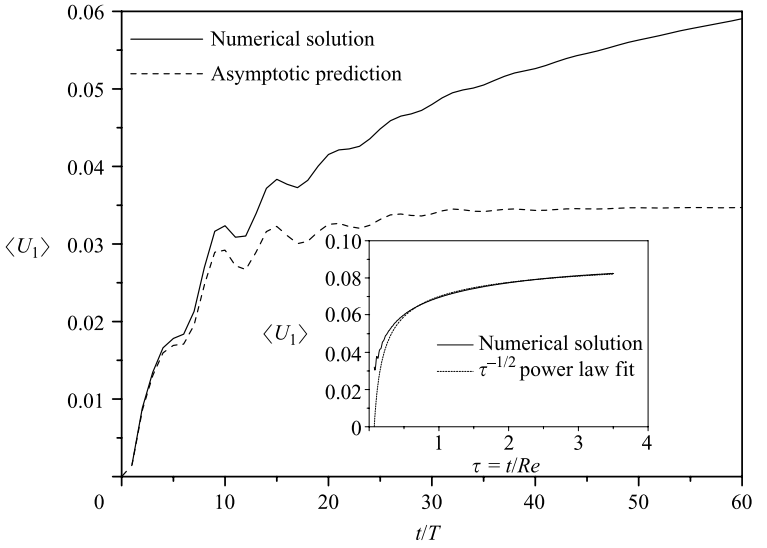

FIGURE 5. Asymptotic and numerical solution for the mean translational velocity of the left-hand bubble averaged over the period of the forcing $T = (1/2)\pi$, $R_{10} = 100\,\mu\text{m}$, when $\varepsilon = 0.05$. In the inset the numerical solution and a fit of the form $A - B/t^{1/2}$ for the average translational velocity are plotted against the long time scale $\tau = t/Re$; $Re = 855$ in this case.

(4.7)–(4.10), the effect of Re on the evolution of vorticity and drift velocity is through the radial motion. The two bubbles are essentially nonlinearly damped oscillators whose average radial velocity, $\langle \mathrm{d}R/\mathrm{d}\tau \rangle$, was systematically found to decay like $\tau^{-3/2}$ in the numerical simulations that were conducted in the present study. This result is corroborated by the multiple-time-scale analysis for damped oscillators, Bender & Orszag (1978). As a result, the average vorticity and translational velocity approach their corresponding steady state like $\tau^{-1/2}$ as $\tau \to \infty$. Thus, inertia imposes the time scale of the radial motion, decelerates the diffusion of vorticity and leads to a larger steady drift velocity, albeit at a slower rate, in comparison with the prediction of the short-time analysis. This was a recurring theme in the present study that explains the discrepancy between our asymptotic and numerical results. A detailed multiple-time-scale analysis was not pursued any further since it would lead to a formulation that would require an equally expensive numerical solution as the one presented in § 3. Furthermore, the theory on which our general model is based, (3.2)–(3.6), would not be valid for very long times, for those cases for which the two bubbles attract each other until coalescence and eventually their distance apart becomes comparable to their radius. In addition, when the variation of the distance between the two bubbles is taken into account they may form a stable pair in a finite time interval, while the distance between them is still much larger than their radii, in which case the asymptotic result remains valid throughout the motion.

The evolution of the translational velocity of the left-hand bubble averaged over a period is given in figure 6(*a–d*) with increasing amplitude of the acoustic disturbance, $\varepsilon = 0.1, 0.25, 0.5, 0.8$, respectively. Figure 6 appears non-smooth because straight lines have been used to connect these averaged values. There is qualitative agreement between the numerical and asymptotic prediction, which is even quantitative in the initial stages of the motion. The tendency for the appearance of a steady drift velocity at the late stages of the motion should also be pointed out. The sign of the drift

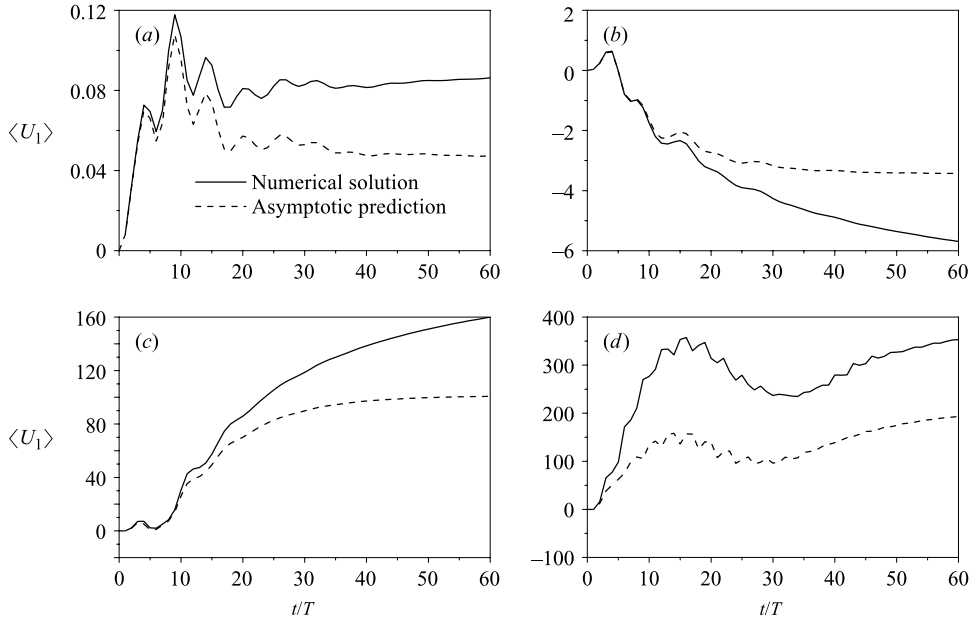

FIGURE 6. Asymptotic and numerical solution of the mean translational velocity of the left-hand bubble, $R_{10} = 100\,\mu$m when (*a*) $\varepsilon = 0.1$, (*b*) $\varepsilon = 0.25$, (*c*) $\varepsilon = 0.5$, (*d*) $\varepsilon = 0.8$.

velocity, however, is strongly dependent on the amplitude of the disturbance. As can be seen from figure 6(*a*, *b*) the average drift velocity becomes repulsive as ε increases from 0.1 to 0.25. The dominance of the second harmonic of the forcing frequency over the rest, particularly when ε becomes 0.25, is clearly demonstrated through the amplitude of the Fourier components (figure 7*a–d*) of the time series of the bubble radius of the left-hand bubble for the cases shown in figure 6. The appearance of the second harmonic, $2\omega_f/2\pi = 33.6$, which falls within the interval $\omega_{10}/2\pi = 33$ kHz, $\omega_{20}/2\pi = 36.5$ kHz, drives the oscillations of the two bubbles out of phase, thus inverting the sign of the average translational velocity, which is also a measure of the secondary Bjerknes forces, causing the bubbles to repel each other. However, as ε further increases and becomes 0.5 and 0.8 the average drift velocity becomes attractive again; see also figure 6(*c*, *d*). Turning to the Fourier components of the radial motion one notices the growth of even higher harmonics, $3\omega_f$, $4\omega_f$, as well as subharmonics, which fall outside the interval defined by the two linear resonance frequencies, ω_{10}, ω_{20}, thus causing the bubbles to attract again.

An interesting aspect of figure 6(*d*) is that the average translational velocity, both numerical and asymptotic, is oscillatory in the time range for which the bubbles undergo clear drifting in figure 6(*a*, *b*, *c*). This attests to the fact that there is more than one time scale determining the motion, and this is verified by the Fourier decomposition of the radial motion of the left-hand bubble when $\varepsilon = 0.8$. In fact, owing to the increased level of nonlinearity, the spectrum is enriched with a number of frequencies that are not exact multiples of the forcing, leading to time scales larger than T_f (subharmonics). This may also explain the increased discrepancy between the numerical and asymptotic prediction, compared to the cases depicted in figure 6(*a*, *b*, *c*) where ε is smaller. Finally, it should be noted that as ε increases, system inertia increases as well and the time needed for a steady drift velocity to be attained increases.

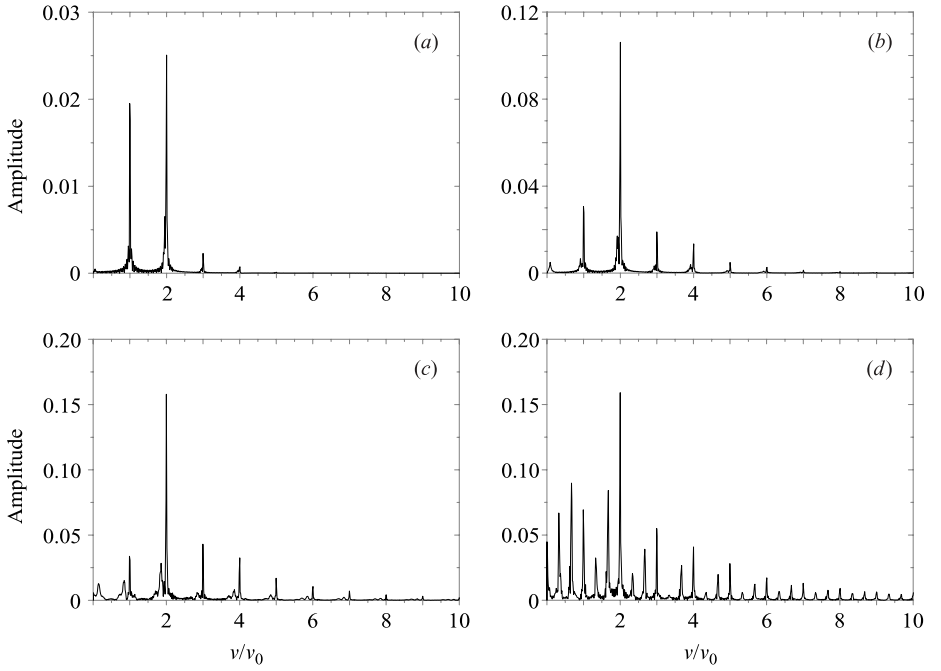

FIGURE 7. Fourier decomposition of the radial velocity of the left-hand bubble, $R_{10} = 100\,\mu\text{m}$, when (*a*) $\varepsilon = 0.1$, (*b*) $\varepsilon = 0.25$, (*c*) $\varepsilon = 0.5$, (*d*) $\varepsilon = 0.8$; ν denotes dimensionless frequency normalized by the dimensionless frequency corresponding to the forcing $\nu_0 = (1/2)/\pi$.

The motion of the right-hand bubble, $R_{20} = 90\,\mu\text{m}$, was also examined. Since all that distinguishes the left- and right-hand bubbles is equilibrium radii, in order to avoid additional coding, equations (3.2)–(3.5) were used, while setting $R_{10} = 90\,\mu\text{m}$ and $R_{20} = 100\,\mu\text{m}$. Then the translational velocity of the bubble with equilibrium radius 90 μm was calculated in the same fashion as that of the bubble with equilibrium radius 100 μm, with the understanding that the translational velocity is made dimensionless via $R_{20}\omega_f(R_{20}/L_0)^2$, where now $R_{20} = 100\,\mu\text{m}$, whereas $R_{20} = 90\,\mu\text{m}$ in the previous calculations. If we call the bubble with equilibrium radius 100 μm the left-hand bubble for the rest of this section and denote its dimensionless translational velocity by U_1, while using U_2 for the dimensionless instantaneous translational velocity of the smaller bubble, then monitoring the evolution of the time derivative of the average translational velocities, $\mathrm{d}\langle U_1\rangle/\mathrm{d}t$, $\mathrm{d}\langle U_2\rangle/\mathrm{d}t$, over a number of periods of the forcing, constitutes a useful check on our numerical or asymptotic solution. Indeed, when viscous dissipation is not very important, the product of average bubble acceleration by the average bubble volume must be the same for both the left- and right-hand bubbles:

$$R_{10}^3 \frac{\mathrm{d}\langle U_1^*\rangle}{\mathrm{d}t} \approx R_{20}^3 \frac{\mathrm{d}\langle U_2^*\rangle}{\mathrm{d}t} \Rightarrow \frac{\mathrm{d}\langle U_1\rangle}{\mathrm{d}t} \approx \frac{\mathrm{d}\langle U_2\rangle}{\mathrm{d}t}. \tag{5.2}$$

The second equality is obtained by rendering the first one dimensionless. This is, in fact, another way to express the original inviscid result by Bjerknes, namely that the average drift velocity of each of two interacting bubbles is due to the oscillations of the other one, hence the action–reaction type average forces exerted upon them as illustrated by (5.2). In the above it is assumed that the equilibrium radii of the two bubbles also represent their mean radius throughout the motion. As will be seen in

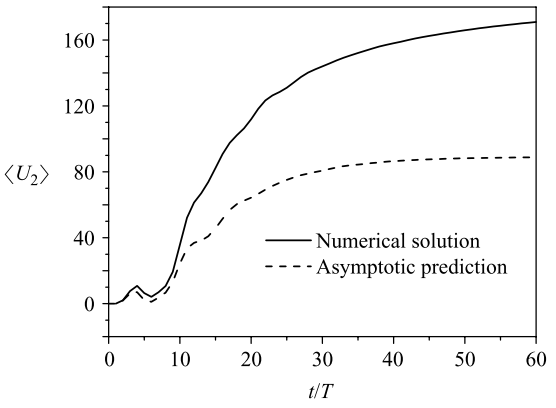

FIGURE 8. Asymptotic and numerical solution of the mean translational velocity of the right-hand bubble, $R_{20} = 90\,\mu\text{m}$ when $\varepsilon = 0.5$.

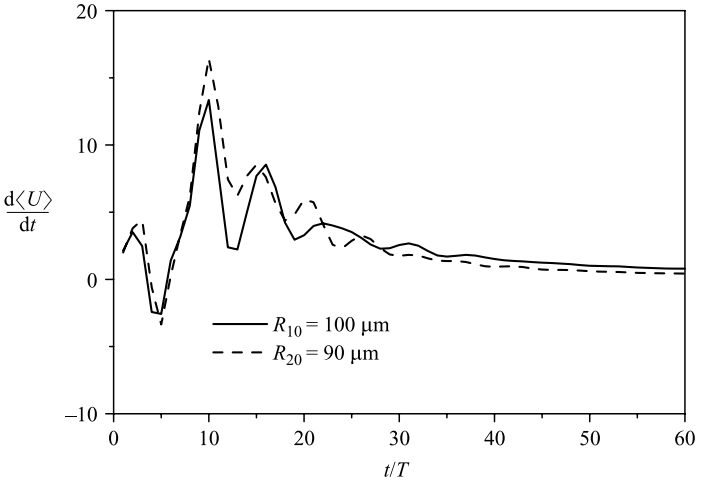

FIGURE 9. Evolution of the mean translational acceleration of the left- and right-hand bubble, $R_{10} = 100\,\mu\text{m}$, $R_{20} = 90\,\mu\text{m}$ $\varepsilon = 0.5$.

the following, (5.2) is not entirely accurate and it deviates from reality as the size of the bubbles decreases or, equivalently, as Re of the motion decreases. Figure 8 shows the evolution of the mean translational velocity of the right-hand bubble, $R_{20} = 90\,\mu\text{m}$, when $\varepsilon = 0.5$ (both numerical solution and asymptotic prediction). Upon comparing with figure 6(c) it is seen that the translational motion of the two bubbles is very similar. In fact, taking the derivative of the average translational velocity of the two bubbles, with respect to the number of elapsed periods of the motion, it turns out that they are almost identical, with the larger left-hand bubble accelerating slightly faster due to its larger Re and, consequently, the smaller drag force it is subjected to, figure 9. It should also be noted that the average acceleration tends to zero as time increases, signalling the appearance of an attractive drift velocity, with the smaller bubble approaching this state faster. This is due to the larger drag force experienced by the smaller bubble, as can be seen by examining Levich's formula for the drag force on the left-hand bubble, (4.20), taken to be the smaller one. Even though the drag force on it is proportional to its size, it also depends on the third

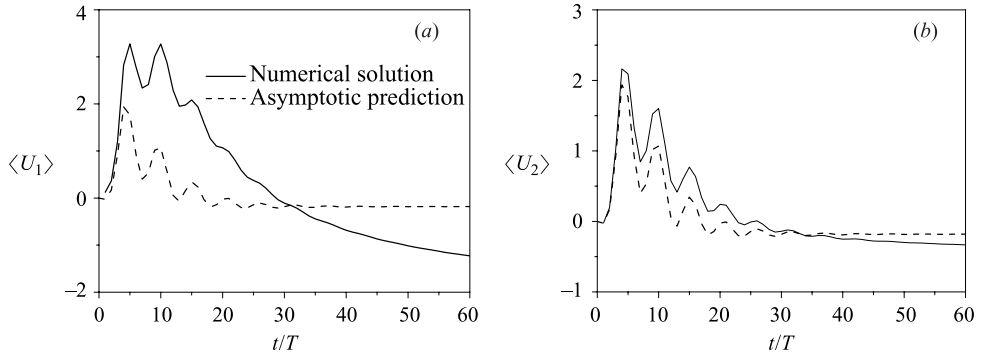

FIGURE 10. Asymptotic and numerical solution of the mean translational velocity of (*a*) the left-hand $R_{10} = 100\,\mu\text{m}$ and (*b*) the right-hand bubble, $R_{20} = 50\,\mu\text{m}$ when $\varepsilon = 0.5$.

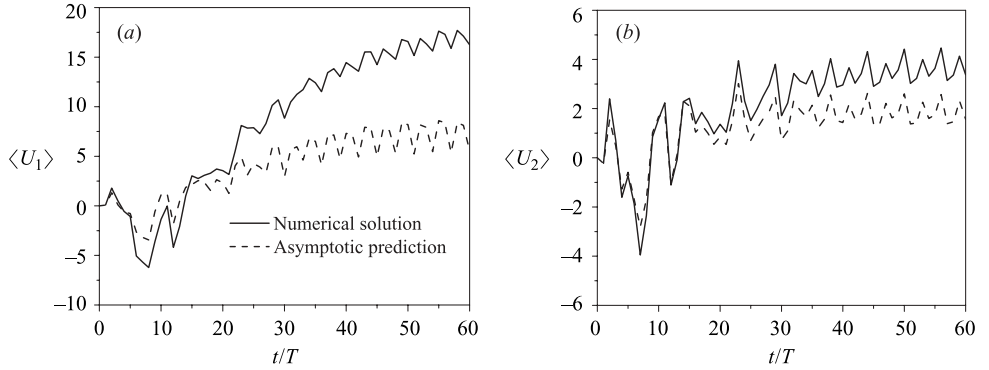

FIGURE 11. Asymptotic and numerical solution of the mean translational velocity of (*a*) the left-hand $R_{10} = 100\,\mu\text{m}$ and (*b*) the right-hand bubble, $R_{20} = 50\,\mu\text{m}$ when $\varepsilon = 0.8$.

power of the radius of the right-hand bubble, via the relative translational velocity U_r^* of the former bubble generated by the oscillations of the latter, thus leading to a larger drag force for the left-hand bubble. This conclusion was also reached by Doinikov (1999a) in his study of two interacting bubbles in a viscous fluid.

The same comparison between the left- and right-hand bubbles was conducted for the case of an even smaller right-hand bubble, $R_{20} = 50\,\mu\text{m}$ setting R_{10} to 100 μm, with ε set to 0.5 and 0.8. An interesting aspect of this comparison is that now a repulsive drift velocity is obtained for the two bubbles even when $\varepsilon = 0.5$, figure 10(*a*, *b*), whereas attractive forces prevail as time increases when ε becomes 0.8, figure 11(*a*, *b*). This reversal is attributed to the fact that $\omega_{20}/2\pi = 66\,\text{kHz}$, in which case both the second harmonic, $2\omega_f/2\pi = 33.6\,\text{kHz}$, and the third harmonic, $3\omega_f/2\pi = 50.4\,\text{kHz}$, of the forcing frequency fall between ω_{10} and ω_{20}, thus widening the range of frequencies for which the bubbles oscillate out of phase and consequently repel each other. When $\varepsilon = 0.8$, growth of even higher harmonics, $4\omega_f/2\pi = 67.2 > \omega_{20}$, re-establishes an attractive secondary Bjerknes force. For all cases a steady drift velocity is approached. Upon comparing the derivative of the average translational velocity of the two bubbles with respect to the number of elapsed periods of the motion we note a similar difference between them as for the previously examined case of two bubbles that are almost equal in size, figure 9. In both cases the left-hand bubble exhibits a larger dimensionless acceleration, towards or away from the other bubble,

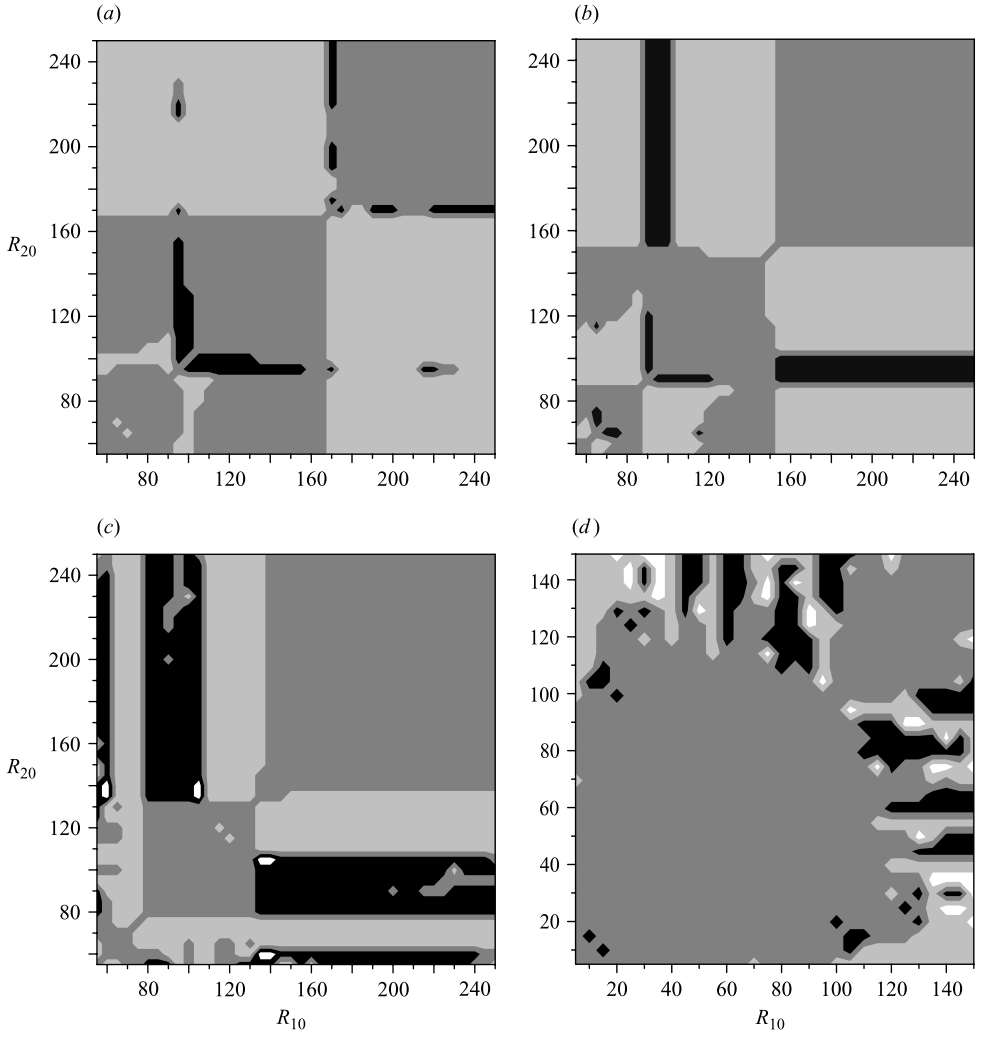

FIGURE 12. Dynamic behaviour of two bubbles that are driven to oscillation by an acoustic wave with forcing frequency, $\omega_f = 16.8$ kHz, and amplitude (*a*) $\varepsilon = 0.25$, (*b*) $\varepsilon = 0.5$, (*c*) $\varepsilon = 0.8$ and (*d*) $\varepsilon = 1.1$. Different regions in the (R_{10}, R_{20})-plane are identified as: ▒, repulsion; ▓, attraction; ■, stable pair after attraction; □, stable pair after repulsion.

due to its larger size. It is for this reason also that the right-hand bubble reaches the steady oscillatory state faster than the left-hand one.

In an attempt to determine the dynamic behaviour of a pair of bubbles with equilibrium radii of the order examined in this section, utilizing the fact that for not very large sound amplitudes the translational part of the motion is described fairly accurately by (4.19), we calculate the dynamic interaction of the binary bubble system for a wide range of sound amplitudes, $0.25 \leqslant \varepsilon \leqslant 1.1$, when the forcing frequency, $\omega_f/(2\pi)$, equals 16.8 kHz and for a very large time frame, 20000 periods of the forcing. Equations (2.16) and (4.19) are employed for each of the two bubbles, resulting in significant savings in computer time since they are both ODEs, in conjunction with (3.6) that describes the time variation of their distance. The outcome of these simulations is shown in figure 12(*a–d*) for the cases with $\varepsilon = 0.25$, 0.5, 0.8 and 1.1,

respectively; a step of 5 μm is used in order to sweep the entire range of equilibrium radii of the two bubbles and the initial distance between the two centres of mass for each simulation is set to be 50 times the larger of the two equilibrium radii. The effect of the second harmonic, which is predicted by Oguz & Prosperetti to grow as ε increases, is indeed important as can be seen from the widening of the light grey regions indicating bubble repulsion in the lower left quadrant of the graphs as ε increases from 0.25 to 0.5, figure 12(a, b). However, as ε increases further this effect is suppressed due to the growth of higher modes, figure 12(c, d), and this is reflected in the predominance of dark grey regions where attractive forces prevail, whether they are purely attractive or leading to stable bubble pairs. Another important aspect of the dynamic behaviour of binary bubble systems is related to the formation of stable bubble pairs, black regions in figure 12(a–d), which is enhanced as the level of nonlinearity increases with increasing ε and occurs primarily in the vicinity of regions corresponding to linear resonance, figure 12(a), as well as higher resonances, figure 12(b, c, d), of the forcing frequency ω_f. As can be seen from figure 12 the resonant bubble size decreases with increasing ε, an effect anticipated by weakly nonlinear theory. In addition, black bands, indicating the formation of a stable pair after attraction, appear in the (R_{10}, R_{20}) plane in regions corresponding to sizes that resonate at superharmonics of ω_f, $2\omega_f$, $3\omega_f$ etc. The possibility of the formation of stable bubble pairs by near resonant bubbles has been recognized by Barbat *et al.* for small-amplitude oscillations. A lucid description of the same effect for inviscid flow is also given by Harkin *et al.* (2001). This effect is extended here to cover higher amplitudes with the difference that smaller sizes are now involved owing to superharmonic resonance. It should also be pointed out that for very large amplitudes, figure 12(d), the possibility of the appearance of stable pairs at even smaller sizes, equilibrium radii on the order of 10 μm, is revealed. As will be seen in the next section this is associated with a nonlinear type of resonance that occurs when the amplitude of sound, ε, exceeds a large value known as the Blake threshold. In this amplitude regime surface tension cannot counterbalance forces of inertia, hence the bubble undergoes oscillations of very large amplitude.

Figure 13(a–f) shows the evolution of the average distance between the centres of mass of the two bubbles in the following situations: (1) the two bubbles are attracted until coalescence, as in figure 13(a) representing a bubble pair that belongs to the dark grey region of figure 12(c); (2) the two bubbles attract each other until stable bubble pairs are formed, as in figure 13(b, c, d) representing bubble pairs that belong to the black region of figure 12(c); (3) the two bubbles constantly repel each other, as in figure 13(e) representing a bubble pair that belongs to the light grey region of figure 12(c); and (4) the two bubbles repel each other until a stable pair is formed, as in figure 13(f) representing a bubble pair that belongs to the white region of figure 12(c). It can be seen that, owing to the large value of ε and, consequently, to the additional time scales that affect the motion, the average distance $\langle D \rangle$ can be oscillatory once a dynamic steady state is reached, figure 13(c). In fact, at the border between regions signifying attraction and formation of stable bubble pairs degenerate dynamic behaviours may be observed, as in figure 13(d) where the two bubbles neither attract nor repel each other, at least within the time frame of the simulations. Rather, they keep oscillating around their initial distance. The situation with constant average distance between the two bubbles, e.g. figure 13(b), pertains to two interacting bubbles of unequal size that are moving in the same direction with the same average translational velocity along the line of centres. In view of the fact that, in the context of inviscid theory, the Bjerknes forces between the two bubbles

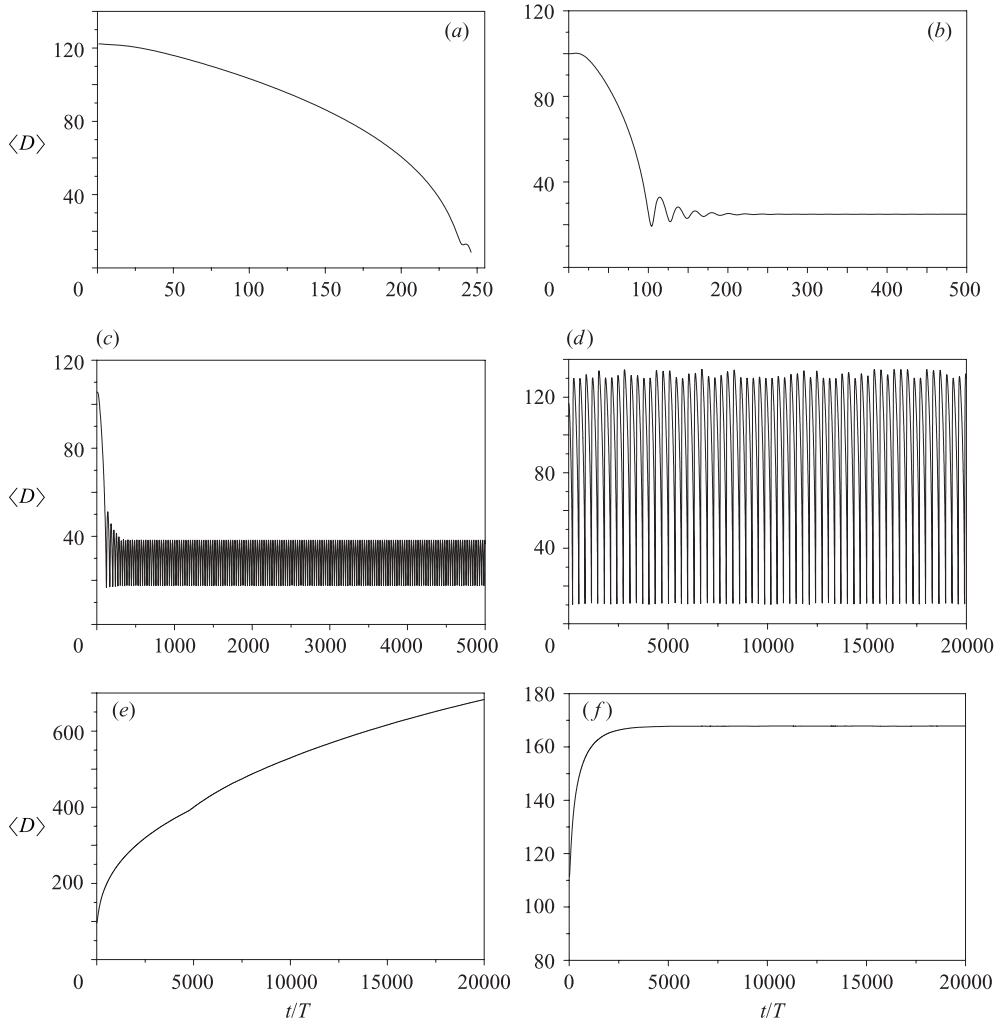

FIGURE 13. Evolution of the average distance between the two centres of mass with increasing number of elapsed cycles of the forcing for (*a*) $R_{10} = 220\,\mu\text{m}$; $R_{20} = 90\,\mu\text{m}$; (*b*) $R_{10} = 180\,\mu\text{m}$, $R_{20} = 90\,\mu\text{m}$; (*c*) $R_{10} = 190\,\mu\text{m}$, $R_{20} = 90\,\mu\text{m}$; (*d*) $R_{10} = 210\,\mu\text{m}$, $R_{20} = 90\,\mu\text{m}$; (*e*) $R_{10} = 135\,\mu\text{m}$, $R_{20} = 70\,\mu\text{m}$; (*f*) $R_{10} = 135\,\mu\text{m}$, $R_{20} = 60\,\mu\text{m}$, $\varepsilon = 0.8$.

are equal in magnitude but opposite in sign this may seem counterintuitive. However, it should be recalled that viscous forces between bubbles of unequal size are not the same in magnitude and, therefore, upon averaging (4.19) for the left- and right-hand bubbles and adding, it can be shown that the total linear momentum of the system is non-zero, in general, thus allowing for flow patterns with the two bubbles moving in the same direction, eventually.

5.2. *Interaction of two bubbles of smaller size,* $R_{i0} \sim 10\,\mu m$

A second set of numerical simulations was conducted following Mettin *et al.* (1997) who attempted to find the mechanism responsible for the formation of acoustic streamers in experiments on multi-bubble sonoluminescence (Ohl *et al.* 1999; Mettin *et al.* 2000). In this case the bubbles are much smaller – R_{i0} is on the order of $10\,\mu\text{m}$ – while they are driven well below resonance, $\omega_f/2\pi = 20\,\text{kHz}$, and at very large

amplitudes, $\varepsilon \sim 1$. The choice of bubble sizes is motivated by experimental bubble size statistics of cavitating water in strong acoustic fields (Billo 1996). It is important to note that, in an effort to evaluate the secondary Bjerknes force at amplitudes near the dynamic Blake threshold ($\varepsilon = 1.3$), Mettin *et al.* (1997) utilized an expression for the average Bjerknes force, (4.2), which is valid in the absence of viscous dissipation and under the assumption that the motion is dominated by the forcing frequency ω_f and its higher harmonics. The present formulation, (3.2)–(3.6), allows us to calculate the translational part of the motion including viscous dissipation for any level of nonlinearity, provided the translational velocity does not become comparable in magnitude with the radial velocity, and to capture any subharmonics that may be excited. As a compromise between the need to account for very intense sound fields, large ε, and maintain the computational cost at a reasonable level we considered values of ε no larger than 1.2, which is smaller than the maximum amplitude used by Mettin *et al.*, but still near the dynamic Blake threshold. In addition, the dimensionless distance between the two centres of mass is taken to be constant in the numerical simulations to be presented in the next few paragraphs. This is done in order to reduce part of the computational effort by decoupling the translational part of the motion of the two bubbles.

Mettin *et al.* discovered sign inversion in the mutual interaction force of two bubbles as the distance between them decreases, which they attributed to a nonlinear resonance experienced by the bubbles at conditions near the Blake threshold. This result is corroborated by the findings of the present study, when the evolution of the radius of the left-hand bubble is calculated for a number of bubble pairs, with the initial distance between them set to 1 mm and kept constant throughout the simulation. The equilibrium radius of the right-hand bubble is set to $R_{20} = 4\,\mu\text{m}$ whereas the equilibrium radius of the left-hand bubble R_{10} is varied between 1 μm and 10 μm; $\varepsilon = 1.2$ and $\omega_f/2\pi = 20\,\text{kHz}$. Indeed, it is seen that the radial motion of the left-hand bubble is periodic, figure 14(*a*), for the case with $R_{10} = 1.0\,\mu\text{m}$, with its period determined by the forcing, $T = 2\pi$. The evolution of the instantaneous translational velocity is shown in figure 14(*b*), for the same conditions. Another important dynamical aspect of the motion in this range of ε values is the fact that the amplitude of the radial position, R_{1max}, increases drastically as the equilibrium radius, R_{10}, increases, figure 15. It is for such large-amplitude disturbances that the far field compressibility is essential in order to obtain meaningful results and avoid premature breakup of the bubble. In fact, when $R_{10} \approx 2.5\,\mu\text{m}$, R_{1max} exhibits an abrupt increase, indicating the appearance of nonlinear resonance, figure 15. It is also seen from figure 15 that the location of this abrupt increase in the maximum radius of the left-hand bubble is shifted to larger equilibrium radii as the distance between the two bubbles decreases to $L = 0.1\,\text{mm}$ whereas R_{1max}/R_1 itself decreases.

At this point it should be stressed that, owing to the very large amplitude of the acoustic disturbance, the instantaneous as well as the average values of the translational velocity increase significantly with increasing equilibrium radius thus rendering the validity of our formulation questionable as this requires that $|\boldsymbol{U}^*_{vi}| \gg |\boldsymbol{U}^*_{pi}|$ or $U_1(R_{20}/L)^2 \gg \dot{R}_1$, with $R_{20} \gg L$. In fact, the ratio between the maximum values of the dimensional instantaneous translational and radial velocities was monitored with increasing equilibrium radius, R_{10}, and it was seen to increase significantly until it became an order one quantity when $R_{10} \sim 3\,\mu\text{m}$ when $L = 1\,\text{mm}$. This is, however, a limitation of all the available theories that are discussed in this paper that treat large-amplitude acoustic interactions between bubbles.

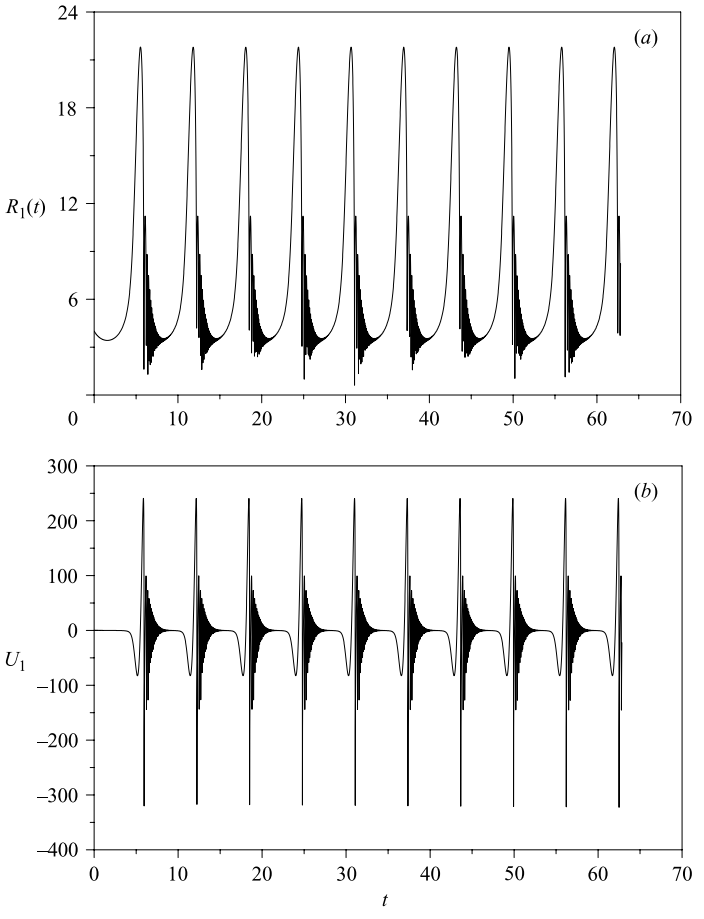

FIGURE 14. Evolution of the instantaneous (*a*) radial position and (*b*) translational velocity of the left-hand bubble, with time; $R_{10} = 1.0\,\mu\text{m}$; $R_{20} = 4\,\mu\text{m}$, $\varepsilon = 1.2$, $\omega_f = 2\pi 20\,\text{kHz}$ and $L = 1\,\text{mm}$.

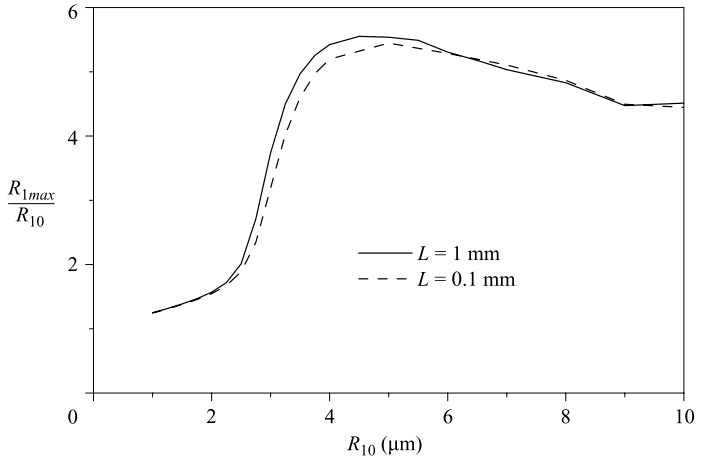

FIGURE 15. Evolution of the maximum radius of the left-hand bubble, R_{1max}, normalized with its equilibrium radius, R_{10}, as the latter increases from 1 to 10 μm and the distance between them, L, varies from 1 to 0.1 mm; $R_{20} = 4\,\mu\text{m}$, $\varepsilon = 1.2$ and $\omega_f = 2\pi 20\,\text{kHz}$.

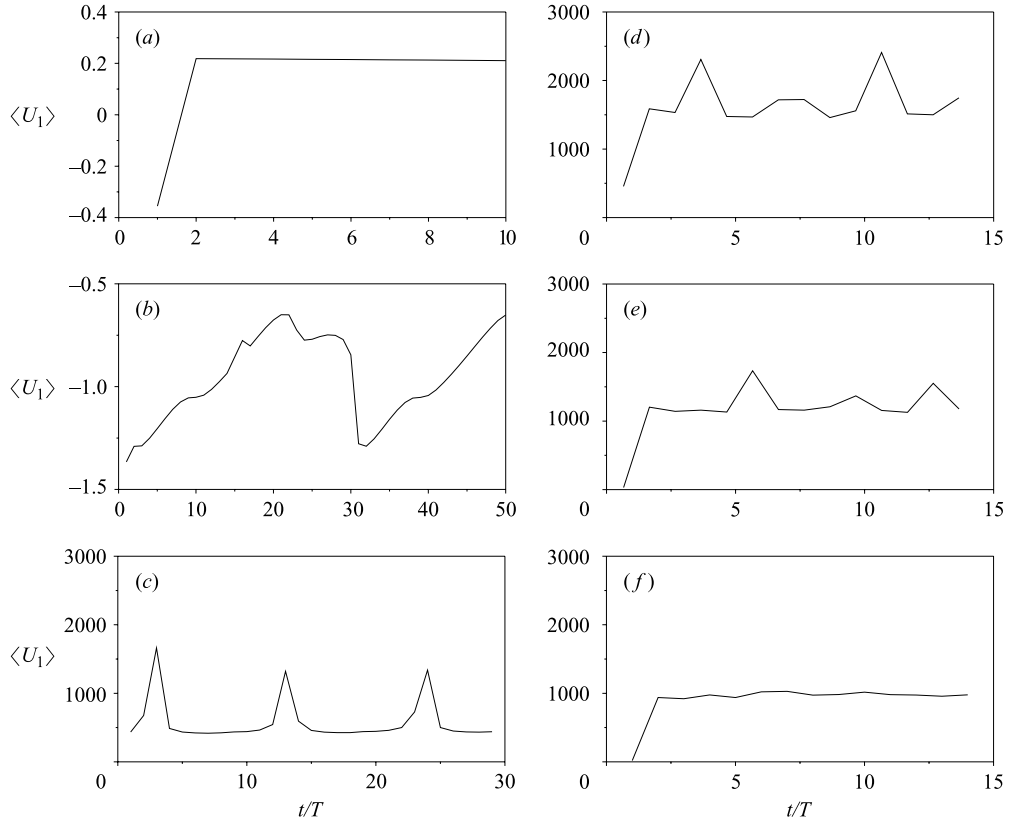

FIGURE 16. Evolution of the mean translational velocity of the left-hand bubble with increasing equilibrium radius R_{10} (*a*) 1.0 μm, (*b*) 2.5 μm, (*c*) 3.5 μm, (*d*) 6.0 μm, (*e*) 8.0 μm, (*f*) 10.0 μm; $R_{20} = 4$ μm, $\varepsilon = 1.2$, $\omega_f = 2\pi 20$ kHz and $L = 1$ mm.

The evolution of the mean value of the translational velocity with increasing number of elapsed periods of the forcing is given for selected pairs of bubbles, $R_{20} = 4$ μm, $1\,\mu\text{m} \leqslant R_{10} \leqslant 10\,\mu\text{m}$, and the same sound field properties, for the left-hand bubble, figure 16, when the initial distance between the two bubbles L_0 is set to 1 mm. The asymptotic result is not shown since for such small bubbles, and small *Re*, it is not expected to be valid. However, it will be seen in the following that the asymptotic result can provide very useful predictions even in the case of small bubbles. For small values of the equilibrium radius of the left-hand bubble, $R_{10} \sim 1$ μm the mean translational velocity is positive and increasing as time elapses until it reaches an almost constant value, the steady drift velocity, corresponding to a dynamic steady state. The steady drift velocity is a result of viscous dissipation and tends to increase with increasing initial radius of the left-hand bubble. It should be noted that the present study allows the appearance of subharmonics as well as frequencies that are not exact multiples of the forcing frequency, as opposed to the analysis by Mettin *et al.* where periodicity determined by the forcing is assumed. This can be seen in the irregularity of the evolution of the average translational velocity shown in figure 16 and in the related Fourier spectra of the instantaneous translational velocity with R_{10} increasing from 1.0 μm to 2.5 and 3.5 μm. The spectrum becomes more and more broadband as R_{10} approaches the resonant size and subharmonics appear mainly

due to the nonlinear interaction between different components of the radial motion entering the calculation of the translational motion. However, most of the energy of the system remains within the forcing frequency and its multiples, which may account for the agreement between results presented here and those of Mettin *et al.* (1997) regarding the sign of the interaction force. Very large attractive average translational velocities are obtained when R_{10} becomes roughly 1.5 μm, turning negative when $R_{10} = 1.75\,\mu\text{m}$. As R_{10} further increases the mean velocity becomes positive again when $R_{10} \approx 2.75\,\mu\text{m}$. This behaviour is due to the nonlinear resonance, shown in figure 15, that occurs when $R_{10} \approx 2.5\,\mu\text{m}$. Attractive average translational velocities persist for equilibrium radii of the left-hand bubble as large as 10 μm. As the equilibrium radius of the left-hand bubble departs from the resonant size the effect of subharmonics becomes weaker and the mean translational velocity tends to recover the pattern of steady oscillation determined solely by the forcing.

When the asymptotic formulation is employed, (2.16) and (4.19) for each bubble along with (3.6), close agreement is achieved with the numerical solution shown in figure 16 for the sign of the average translational velocity. This is not shown for conciseness, but it can be explained by noting that for such large amplitudes the proper characteristic length scale in the definition of *Re* is not the equilibrium radius of one of the two bubbles. Rather, the maximum radius is more representative of the radial motion, which results in a larger effective *Re* and consequently extends the validity of the large-*Re* asymptotic solution to smaller equilibrium radii. A physical explanation for this effect is provided by Reddy & Szeri (2003). They attribute the relevance of the maximum radius to the fact that for intense bubble oscillations most of the translation of its centre of mass coincides with bubble collapse. This is demonstrated by the instantaneous translational velocity of the left-hand bubble, figure 14(*b*), showing the radial pulsations of the bubble.

The evolution of the mean velocity of the right-hand bubble on increasing the equilibrium radius of the left-hand one was also calculated when $L = 1$ mm. For convenience, the problem is formulated so that the radius of the left-hand bubble is set to $R_{10} = 4\,\mu\text{m}$ whereas the equilibrium radius of the right-hand bubble is varied between 1 μm and 10 μm. The same pattern of a narrow region of repulsion is obtained when the equilibrium radius of the right-hand bubble is in the interval $1.75\,\mu\text{m} \leqslant R_{20} \leqslant 3.0\,\mu\text{m}$. Note that this interval is slightly shifted towards larger values compared to that obtained when the equilibrium radius of the left-hand bubble, R_{10}, is varied, see figure 16. This asymmetry is attributed to the larger size of the left-hand bubble in the former case and consequently the smaller drag force. When the distance between the two bubbles is decreased to 0.1 mm the average translational velocity of the left-hand bubble remains positive until $R_{10} = 2.75\,\mu\text{m}$. Then there is a much narrower region of repulsion, until $R_{10} = 3.0\,\mu\text{m}$, beyond which it becomes attractive again. Consequently, there is a sign inversion in the Bjerknes force between the bubbles as their distance decreases, indicating the attainment of a stable distance between the two bubbles that prevents them from approaching any further.

In view of the extended validity of the asymptotic formulation presented in § 4 for the case of micro-bubbles oscillating well within the nonlinear regime and in order to reduce the computational cost, the dynamic behaviour of a pair of acoustically driven bubbles, with equilibrium radii on the order of 10 μm, is investigated when the amplitude of the acoustic disturbance is on the order of the Blake threshold, $1.1 \leqslant \varepsilon \leqslant 1.3$, its forcing frequency $\omega_f = 20\,\text{kHz}$ and the initial inter-bubble distance 1 mm. The simulations span a time interval of 8000 periods of the forcing frequency, which amounts to a duration of 0.4 s. This time frame is much longer than the

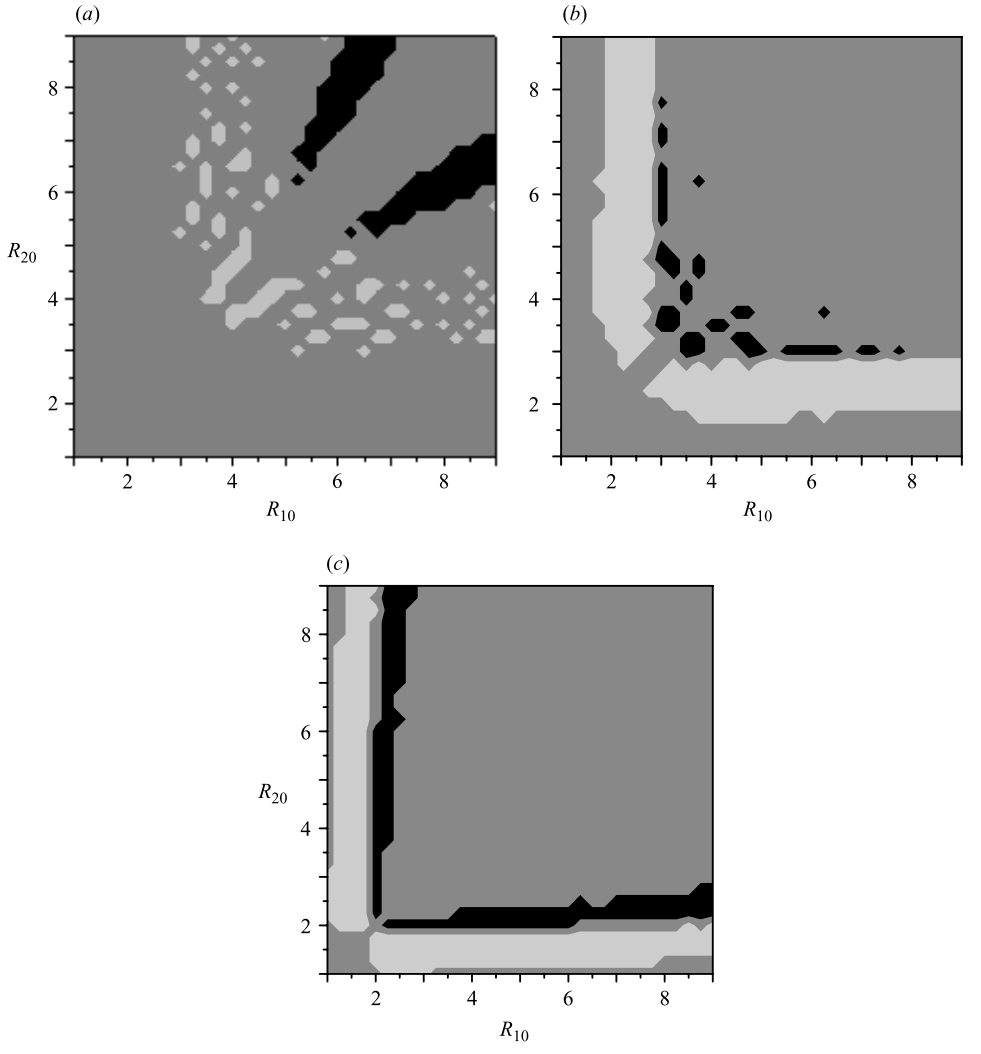

FIGURE 17. Dynamic behaviour of two bubbles that are driven to oscillation by an acoustic wave with forcing frequency, $\omega_f = 20\,\mathrm{kHz}$, and amplitude (*a*) $\varepsilon = 1.1$, (*b*) $\varepsilon = 1.2$ and (*c*) $\varepsilon = 1.3$. Different regions in the (R_{10}, R_{20})-plane are identified as: ▫, repulsion, ▪ attraction, ■ stable pair.

time scale over which acoustic streamers are formed in experimental investigations (Mettin *et al.* 2000). A step of 0.25 μm is used in order to sweep the entire range of equilibrium radii of the two bubbles and the dynamic behaviour of the two-bubble system is classified in the same fashion as in figure 12. As can be seen from figure 17(*a*), the case with $\varepsilon = 1.1$ is simply a blow-up of the small equilibrium radii region in figure 12(*d*) without a clearly formed pattern of black regions that correspond to stable bubble pairs. As ε increases, figure 17(*b*, *c*) corresponding to $\varepsilon = 1.2$ and 1.3, a pattern that is very similar to that observed in the case of near linear resonance, figures 12(*a*, *b*, *c*), in the neighbourhood of resonant sizes is captured in the vicinity of an equilibrium radius of 2 μm corresponding to the Blake threshold. These findings are in qualitative agreement with the results of numerical simulations for the average translational velocity of the left- and right-hand bubbles when the distance between

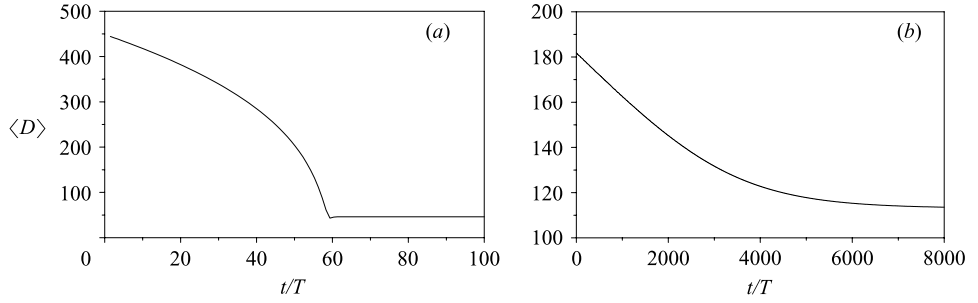

FIGURE 18. Evolution of the average distance between the two centres of mass with increasing number of elapsed cycles of the forcing for (*a*) $R_{10} = 4\,\mu\text{m}$, $R_{20} = 2.25\,\mu\text{m}$; (*b*) $R_{10} = 2\,\mu\text{m}$, $R_{20} = 5.5\,\mu\text{m}$, $\varepsilon = 1.3$.

their centres of mass is fixed, and point out the importance of resonance for the formation of acoustic streamers even in the strongly nonlinear regime. The evolution of the average bubble distance with the number of elapsed cycles of the forcing ferquency is shown in figure 18(*a*, *b*) for selected bubble pairs. It should be noted that the final average distances as well as the time scales over which they are achieved are comparable with those recorded in experiments and that as time increases slower moving bubbles become candidates for the formation of stable pairs since it takes longer for viscosity to decelerate their motion and produce the steady drift velocity.

6. Conclusions

A systematic effort was made to evaluate the two available mechanisms that explain the formation of stable bubble clusters when bubbles are oscillated below resonance with an intense acoustic disturbance. The mechanism attributing this effect to nonlinear growth of the second harmonic of the forcing frequency, proposed by Oguz & Prosperetti (1990), was verified numerically and asymptotically, in the limit of large *Re* based on the radial motion of relatively large bubbles, and extended to include a wider range of amplitudes when the size discrepancy between the two bubbles is large. Subsequently, it was found that as the amplitude further increases this mechanism predicts attraction due to the appearance of higher harmonics that fall outside the interval defined by the eigenfrequencies of the two bubbles. The mechanism identified as being responsible for the formation of acoustic streamers in large populations of micro-bubbles by Mettin *et al.* (1997), namely that as the distance between the two bubbles decreases there is a sign inversion in the Bjerknes force between them as a result of a nonlinear resonance near the Blake threshold (see figure 3*c*, *d* in their study), has also been verified by the findings of the present study, to the extent of its validity. The basic features that appear to be necessary for the formation of stable bubble pairs for both micro-bubbles and relatively large bubbles are those of resonance, whether it refers to the primary and secondary resonances in the linear case or to the nonlinear resonance situation that arises near the Blake threshold, and nonlinearity. The importance of near resonant conditions was also pointed out by Barbat *et al.* (1999) and Harkin *et al.* (2001) for bubbles with equilibrium sizes on the order of $100\,\mu\text{m}$ that interact in a weak field. In the experimental observations by Mettin *et al.* (2000), however, acoustic streamers of micro-bubbles only are observed owing to the very large sound amplitude which, probably, destroys larger bubbles through violent shape oscillations. Under

milder conditions and for the appropriate range of equilibrium radii, so that shape instabilities are removed or at least considerably delayed, it is expected that even larger bubbles should be observed to form such patterns.

It was also seen that, for the case of water, viscous damping does not significantly alter the findings of potential theory, its main effects being that (*a*) it may eventually lead to a 'terminal' drift velocity that is oscillating with the forcing frequency and consequently to a constant average distance between the two bubbles and (*b*) it breaks the symmetry of the Bjerknes forces, for bubbles of unequal size, owing to its non-conservative nature. The fact that viscous damping has a minor effect on the translational motion of two bubbles at large or moderate separations is corroborated by the experimental findings of Barbat *et al.* (1999). Nevertheless, the numerical procedure that was developed here is valid for any Reynolds number and is expected to be very useful when more viscous fluids, like glycerine, are considered. In addition, an asymptotic solution was obtained that accounts for viscous dissipation and provides an $O(1/Re)$ correction to the translational motion of the two bubbles. It is basically the Levich expression for the drag coefficient for flow around a spherical bubble and is valid when the Reynolds number, based on the radial motion of the bubble, is very large. Interestingly, for very large sound amplitudes, this expression works quite well even for bubbles with very small equilibrium radii because in this case it is the maximum bubble radius that characterizes the translational part of the motion. It should be stressed that the validity of this asymptotic prediction is restricted to $\tau = t/Re$ being a small or at the most an order one quantity. For very long times the evolution of the average translational velocity is governed by the $\tau^{-1/2}$ transient that is commonly observed in dissipative processes.

Overall, the mechanism based on nonlinear resonance (Blake threshold) seems to be closer to reality, without being entirely satisfactory in view of the relative narrow range that it predicts for the formation of stable pairs of bubbles. Acoustic streamers are met so often that one might expect a wider range. Of course, as the amplitude of the acoustic disturbance becomes larger, it is expected that the formation of bubble pairs will be enhanced, see also figures 12 and 17, and that as time advances the possibility for the formation of stable bubble pairs increases. Unfortunately, both of the mechanisms that are mentioned in the literature as well as the approach adopted in the present study suffer from the drawback that for amplitudes near the Blake threshold one of their central assumptions, namely that the translational velocity must be less dominant than the radial one, is violated. In order to remedy this limitation of the theory an improved formulation is needed that can handle smaller inter-bubble distances as well as situations where the instantaneous radial and translational velocities of the bubbles are comparable in size. To this end the approach adopted by Pelekasis & Tsamopoulos (1993*a*, *b*) in their study of inviscid bubble–bubble interactions may be extended in the future to account for weak viscous effects, following the method developed by Lundgren & Mansour (1988) for the study of drop oscillations. Finally, it would also be instructive to examine the situation with the primary Bjerknes force acting in the same direction as the secondary one, as opposed to being perpendicular to the secondary Bjerknes force as was assumed in the present study. This arrangement is closer to the pattern observed in experiments where the filamentary bubble structures are clearly seen to approach the pressure antinode of the resonator.

All the authors wish to acknowledge their financial support under the INCO Program of DG 12 (N° IC15-CT98-0141). N. A. P. and J. A. T. acknowledge the

support by the Ministry of education of Greece under the EPEAEK Program. A. D. acknowledges financial support during his stay in Greece for two months in 1999 under the NATO Science Fellowships Program.

REFERENCES

Barbat, T., Ashgriz, N. & Liu, C.-S. 1999 Dynamics of two interacting bubbles in an acoustic field. *J. Fluid Mech.* **389**, 137–168.

Batchelor, G. K. 1967 *An Introduction to Fluid Dynamics*. Cambridge University Press.

Bender, C. M. & Orszag, S. A. 1978 *Advanced Mathematical Methods for Scientists and Engineers*. McGraw-Hill.

Billo, A. 1996 Holographische Partikelfeldanalyse am Beispiel akustischer Lichtenberg-Figuren (English translation: Application of holographic particle field analysis on acoustic Lichtenberg figures.) PhD thesis, TH Darmstadt, Germany.

Bjerknes, V. F. K. 1906 *Fields of Force*. Columbia University Press.

Crum, L. A. 1975 Bjerknes forces on bubbles in a stationary sound field. *J. Acoust. Soc. Am.* **57**, 1363–1370.

Crum, L. A. & Nordling, D. A. 1972 Velocity of transient cavities in an acoustic stationary wave. *J. Acoust. Soc. Am.* **52**, 294–301.

Doinikov, A. A. 1999*a* Bjerknes forces between two bubbles in a viscous fluid. *J. Acoust. Soc. Am.* **106**, 3305–3312.

Doinikov, A. A. 1999*b* Effects of the second harmonic on the secondary Bjerknes force. *Phys. Rev.* E **59**, 3016–3021.

Doinikov, A. A. & Zavtrak, S. T. 1995 On the mutual interaction of two gas bubbles in a sound field. *Phys. Fluids* **7**, 1923–1930.

Fyrillas, M. M. & Szeri, A. J. 1994 Dissolution or growth of soluble spherical oscillating bubbles. *J. Fluid Mech.* **277**, 381–407.

Haberman, W. L. & Morton, R. H. 1953 An experimental investigation of the drag and shape of air bubbles rising in various liquids. *David Taylor Model Basin Rep.* 802.

Harkin, A., Kaper, T. J. & Nadim A. 2001 Coupled pulsation and translation of two gas bubbles in a liquid. *J. Fluid Mech.* **445**, 377–411.

Keller, J. B. & Miksis, M. 1980 Bubble oscillations of large amplitude. *J. Acoust. Soc. Am.* **68**, 628–633, 1980.

Kobelev, Y. A., Ostrovsky, L. A. & Sutin, A. M. 1979 Effect of self-clearing for acoustic waves in a liquid with gas bubbles. *Pis'ma Zh. Eksp. Teor. Fiz.* **30**, 423.

Landau, L. D. & Lifshitz, E. M. 1959 *Fluid Mechanics*. Pergamon.

Leighton, T. G. 1994 *The Acoustic Bubble*. Academic.

Levich, V. G. 1962 *Physicochemical Hydrodynamics*. Prentice Hall.

Lundgren, T. S. & Mansour, N. N. 1988 Oscillation of drops in zero gravity with weak viscous effects. *J. Fluid Mech.* **194**, 479–510.

Magnaudet, J. & Legendre, D. 1998 The viscous drag force on a spherical bubble with a time dependent radius. *Phys. Fluids* **10**, 550–554.

Mettin, R., Akhatov, I., Parlitz, U., Ohl, C. D., & Lauterborn, W. 1997 Bjerknes forces between small cavitation bubbles in a strong acoustic field. *Phys. Rev.* E **56**, 2924–2931.

Mettin, R., Luther, S., Lindau, O., Koch, P. & Lauterborn, W. 2000 Investigation of cavitation bubble dynamics by means of fast cinematography. In *Dynamics of Multiphase Systems – Proc. Intl Conf. Multiphase Systems ICMS 2000* (ed. M. Ilgamov, I. Akhatov & S. Urmancheev) Ufa (Russia), pp. 279–287.

Minnaert, M. 1933 On musical air bubbles and the sounds of running water. *Phil. Mag.* **16**, 235–248.

Moore, D. W. 1963 The boundary layer on a spherical gas bubble. *J. Fluid Mech.* **16**, 161–176.

Oguz, H. & Prosperetti, A. 1990 A generalization of the impulse and virial theorems with an application to bubble oscillations. *J. Fluid. Mech.* **218**, 143–162.

Ohl, C. D., Kurz, T., Geisler, R., Lindau, O. & Lauterborn, W. 1999 Bubble dynamics, shock waves and sonoluminescence. *Phil. Trans. R. Soc. Lond.* A **357**, 269–294.

Pelekasis, N. A. & Tsamopoulos, J. A. 1993*a* Bjerknes forces between two bubbles Part 1. Response to a step change in pressure. *J. Fluid Mech.* **254**, 467–499.

Pelekasis, N. A. & Tsamopoulos, J. A. 1993*b* Bjerknes forces between two bubbles Part 2. Response to an oscillatory pressure field. *J. Fluid Mech.* **254**, 501–527.

Pelekasis, N. A., Tsamopoulos, J. A. & Manolis, G. D. 1992 A hybrid finite-boundary element method for inviscid flows with free surface. *J. Comput. Phys.* **254**, 501–527.

Pozrikidis, C. 1997 *Introduction to Theoretical and Computational Fluid Dynamics*. Oxford University Press.

Prosperetti, A. & Lezzi, A. 1986 Bubble dynamics in a compressible liquid. Part 1. First-order theory. *J. Fluid Mech.* **168**, 457–478.

Reddy, A. J. & Szeri, A. J. 2003 Coupled dynamics of translation and collapse of acoustically driven microbubbles. *J. Acoust. Soc. Am.* (Submitted).

Slavchev, S. G. & Simeonov, G. 1979 The unsteady boundary layer on a spherical gas bubble. *Z. Angew. Math. Mech.* **59**, 43–50.

Zabolotskaya, E. A. 1984 Interaction of gas bubbles in a sound wave field. *Sov. Phys. Acoust.* **30**, 365–368.